



**HAL**  
open science

## From Diffusion MRI to Brain Connectomics

Aurobrata Ghosh, Rachid Deriche

► **To cite this version:**

Aurobrata Ghosh, Rachid Deriche. From Diffusion MRI to Brain Connectomics. Cazals, Frédéric and Kornprobst, Pierre. Modeling in Computational Biology and Biomedicine: A Multidisciplinary Endeavor, Springer, pp.193-234, 2013, 978-3-642-31208-3. 10.1007/978-3-642-31208-3 . hal-00667912

**HAL Id: hal-00667912**

**<https://inria.hal.science/hal-00667912>**

Submitted on 8 Feb 2012

**HAL** is a multi-disciplinary open access archive for the deposit and dissemination of scientific research documents, whether they are published or not. The documents may come from teaching and research institutions in France or abroad, or from public or private research centers.

L'archive ouverte pluridisciplinaire **HAL**, est destinée au dépôt et à la diffusion de documents scientifiques de niveau recherche, publiés ou non, émanant des établissements d'enseignement et de recherche français ou étrangers, des laboratoires publics ou privés.

# My chapter



# 2 Contents

3	<b>1 From Diffusion MRI to Brain Connectomics</b> . . . . .	vii
4	Aurobrata Ghosh and Rachid Deriche	
5	1.1 Introduction . . . . .	vii
6	1.1.1 The Central Nervous System . . . . .	viii
7	1.1.2 In Vivo CNS Connectivity . . . . .	viii
8	1.1.3 Organization of the Chapter: . . . . .	ix
9	1.2 A Brief History of NMR and MRI . . . . .	x
10	1.3 Nuclear Magnetic Resonance & Diffusion . . . . .	xi
11	1.3.1 The Hahn Spin Echo Experiment . . . . .	xii
12	1.3.2 Diffusion . . . . .	xiii
13	1.3.3 The Stejskal-Tanner PGSE Experiment . . . . .	xv
14	1.3.4 Narrow Gradient Pulse PGSE: q-space Formalism . . . . .	xvi
15	1.4 From Diffusion MRI to Tissue Microstructure . . . . .	xvii
16	1.4.1 Diffusion Tensor Imaging: The Simplest Model . . . . .	xviii
17	1.4.2 Beyond DTI . . . . .	xx
18	1.5 Computational Framework for Processing Diffusion MR Images . . . . .	xxii
19	1.5.1 The Affine Invariant Riemannian Metric for Diffusion Tensors . . . . .	xxiii
20	1.5.2 Estimation of DTs in $Sym_3^+$ Using the Riemannian Metric . . . . .	xxiii
21	1.5.3 Segmentation of a Tensor Field . . . . .	xxiv
22	1.6 Tractography: Inferring the Connectivity . . . . .	xxv
23	1.6.1 Deterministic Tractography . . . . .	xxv
24	1.6.2 Probabilistic Tractography . . . . .	xxvi
25	1.7 Clinical Applications . . . . .	xxvii
26	1.8 Conclusion . . . . .	xxix
27	1.9 Online Resources: Softwares and Databases . . . . .	xxx
28	References . . . . .	xxxii
29	<b>Index</b> . . . . .	xxxv
30	X	



# Chapter 1

## From Diffusion MRI to Brain Connectomics

Aurobrata Ghosh and Rachid Deriche

1. commentaire # 1
2. commentaire # 2
3. ...

**Abstract** Diffusion MRI (dMRI) is a unique modality of MRI which allows one to indirectly examine the microstructure and integrity of the cerebral white matter *in vivo* and *non-invasively*. Its success lies in its capacity to reconstruct the axonal connectivity of the neurons, albeit at a coarser resolution, without having to operate on the patient, which can cause radical alterations to the patient’s cognition. Thus dMRI is beginning to assume a central role in studying and diagnosing important pathologies of the cerebral white matter, such as Alzheimer’s and Parkinson’s diseases, as well as in studying its physical structure *in vivo*. In this chapter we present an overview of the mathematical tools that form the framework of dMRI – from modelling the MRI signal and measuring diffusion properties, to reconstructing the axonal connectivity of the cerebral white matter, i.e., from Diffusion Weighted Images (DWIs) to the human connectome.

### 1.1 Introduction

The main objective of this chapter is to present some mathematical models and computational tools for analyzing and modeling the complex central nervous system’s (brain and spinal cord) neural connectivity. These models and tools will help to better understand the white matter architecture of the human *central nervous system* (CNS) and in a long term, will also help in addressing important and challenging clinical and neuroscience questions. Indeed, due to our aging society, diseases like Alzheimer’s, Parkinson’s disease (PD) and depression will affect a large population. These examples of CNS diseases as well as others, like multiple sclerosis have characteristic abnormalities in the microstructure of brain’s tissues such as its white matter, which are not apparent and cannot be revealed reliably by standard imaging techniques. Diffusion Magnetic Resonance Imaging (dMRI), a recent imaging modality based on the measurement of the random thermal movement (diffusion) of water molecules within samples, can make visible these co-lateral damages to the fibers of the CNS white matter that connect different brain regions. This is why in this chapter, dMRI is the major anatomical imaging modality that will be considered to recover the neural connectivity in the CNS.

We begin this chapter by presenting the CNS, in particular the brain, before delving into the mathematical framework for dMRI. Section 1.1 is dedicated to a perusal of its general structure and organization, the tissues constituting it, and in highlight, the brain’s major neuronal pathways interconnecting its various regions. It aims to provide a context for understanding the general physical problem dMRI attempts to solve.

---

Aurobrata Ghosh  
Athena project-team, INRIA Sophia Antipolis Méditerranée, e-mail: [aurobrata.ghosh@inria.fr](mailto:aurobrata.ghosh@inria.fr)

Rachid Deriche  
Athena project-team, INRIA Sophia Antipolis Méditerranée, e-mail: [rachid.deriche@inria.fr](mailto:rachid.deriche@inria.fr)

### 65 **1.1.1 The Central Nervous System**

66 The human nervous system can be divided into the CNS, which consists of the brain and spinal cord and  
 67 the *peripheral nervous system* (PNS) which consists of the cranial and spinal nerves and their ganglia.

68 The CNS is the largest part of the nervous system and is composed of the spinal cord and the brain  
 69 which comprises a lower part, the brainstem, and an upper part, the prosencephalon or forebrain composed  
 70 of two main units. One is known as the diencephalon. It is located in the midline of the brain and contains  
 71 the thalamus and the hypothalamus. The other is called the telencephalon or cerebrum and holds the  
 72 lateral ventricles, the basal ganglia and the cerebral cortex. The brainstem is also composed of two units:  
 73 the mesencephalon or midbrain and the rhombencephalon or hindbrain which connects the forebrain and  
 74 midbrain to the spinal cord.

75 The nervous system is made of about 100 billion nerve cells, or neurons, able to generate and propagate  
 76 electrical signals to process and transmit neural information. Neurons can receive electrical stimulation  
 77 from other neurons on their soma, through their multiple dendrites. They can integrate this information  
 78 and propagate it to more or less distant locations of the cerebrum by an extension called an axon. Nerve  
 79 signal communication is performed at specialized loci called synapses. Each neuron has on average 1000  
 80 synaptic connections with other neurons. This yields about 100 trillion connections within a human brain.  
 81 All these synapses result in an impressively dense and complex network between functional areas, which  
 82 can be understood as aggregates of nerve cells' soma and dendrites. They are essentially located in the  
 83 grey matter while the underlying wiring constitutes the white matter. According to the connectionist  
 84 point of view, the human brain is organized into distinct processing regions interconnected by a network  
 85 of anatomical relays. Processing units handle the execution of primary cognitive functions, and higher  
 86 cognitive tasks arise from a global coordination between these processing units. Neural signal is processed  
 87 in the cerebral cortex and transmitted to various regions of the brain through the white matter. So we  
 88 distinguish:

- 89 • The *grey matter* essentially forms the outer part of the cerebrum, some nuclei within the brain, as  
 90 well as the deeper part of the spinal cord. It is made of neurons and their unmyelinated fibers. The  
 91 cerebral cortex is the most important structure of the grey matter and plays a major role in various  
 92 functions such as memory, attention and language.
- 93 • *White matter* is composed of axonal nerve fibers, covered by a myelin sheath giving its distinctive  
 94 colour in MRI. It is found in the inner layer of the cortex, the optic nerves, the central and lower areas  
 95 of the brain and surrounding the central shaft of grey matter in the spinal cord.

96 The CNS white matter axons can be distributed diffusely or concentrated in bundles, also referred to as  
 97 tracts or fiber pathways. The brain's white matter pathways are generally categorized into commissural,  
 98 association and projection fibers, depending on the areas they connect (see Fig. 1.1).

- 99 • The *commissural tracts* connect a region in one hemisphere to another region of the opposite hemi-  
 100 sphere.
- 101 • The *association tracts* connect various cortical areas within a given hemisphere.
- 102 • The *projection tracts* connect the cortex to deep brain regions such as the thalamus or the spinal cord.

103 In the spinal cord, it is the grey matter that is located in the center with a typical H-shaped appearance  
 104 in transverse sections. It is surrounded by white matter which contains long ascending and descending  
 105 pathways.

### 106 **1.1.2 In Vivo CNS Connectivity**

107 Compared to the understanding of neural circuitry in animals as cats or mice where the use of invasive  
 108 tracers is possible [59], the knowledge of the human brain organization is relatively poor. Therefore,  
 109 how to study the connectivity information about the CNS anatomy, in particular, about the cerebral  
 110 and spinal cord white matter? Anatomical MRI allows us to distinguish and classify grey matter and  
 111 white matter. However, with this contrast, white matter retains a homogeneous aspect, preventing any  
 112 observation of neural fibers and thus of neuronal connectivity. Cerebral and spinal dissection used to be  
 113 the only means of accessing the neural architecture [22, 30, 74]. Then, anatomists started using chemical  
 114 markers to do neuronography [55, 59]. More recently, neural fiber tractography based on local injection of

chemical markers and subsequent observation of the induced propagation yielded high-quality connectivity mapping in the cat and monkey cerebral cortices [75, 59].

The relatively recent development of dMRI, which uses the orientational preference of water molecules in diffusing along the directions of the fibers has brought in the last twenty years great hopes for the non-invasive exploration of the neural anatomy of the CNS. Indeed dMRI provides a non-invasive way of estimating in vivo CNS fiber structures using the average random thermal movement (diffusion) of water molecules as a probe. Diffusion MRI is a field of research with a history of roughly three decades. It was introduced in the mid 80's by Le Bihan et al. [39], Merboldt et al. [43] and Taylor et al. [63]. As of today, it is the unique non-invasive technique capable of describing the neural connectivity in vivo by quantifying the anisotropic diffusion of water molecules in biological tissues. The great success of dMRI comes from its ability to accurately describe the geometry of the underlying microstructure and to probe the structure of the biological tissue at scales much smaller than the imaging resolution.

The diffusion of water molecules is Gaussian in an isotropic medium and under normal unhindered conditions, but in fibrous structure such as white matter, the diffusion is very often directionally biased or anisotropic and water molecules tend to diffuse along fibers. For example, a molecule inside the axon of a neuron has a low probability to cross a myelin membrane. Therefore the molecule will move principally along the axis of the neural fiber. Conversely if we know that molecules diffuse locally principally in one direction, we can infer that this corresponds to a set of fibers.

### 1.1.3 Organization of the Chapter:

Section 1.2 briefly covers the historical development of Nuclear Magnetic Resonance (NMR) and MRI to set the stage. We explore the physics of the signal generation in NMR and how diffusion properties can be measured non-invasively from NMR in Sect. 1.3. Section 1.3 begins by presenting the fundamental ideas of NMR. Section 1.3.1 then presents the crucial spin echo experiment proposed by Hahn, which is a corner stone experiment that led to the development of diffusion NMR. Next in Sect. 1.3.2 we describe diffusion in considerable detail. Section 1.3.3 then presents the pulse-field-spin-echo (PGSE) experiment that was proposed by Stejskal and Tanner. This important experiment is the modern and practical approach for measuring diffusion from NMR. The Stejskal-Tanner model for the diffusion NMR signal is based on Fick's laws of diffusion. Section 1.3.4 presents next the q-space approach for modelling the diffusion NMR signal, which is based on Einstein's random walk approach to Brownian motion.

Section 1.4 is dedicated to dMRI reconstruction algorithms that allow to go beyond simply measuring intrinsic diffusion properties from NMR/MRI to inferring the microstructure of the underlying tissue non-invasively. Section 1.4.1 presents diffusion tensor imaging (DTI), the most widely used dMRI algorithm with the simplest experimental requirements, but with powerful applications. DTI is however limited under certain microstructure configurations. Section 1.4.2.1 presents diffusion spectrum imaging (DSI), which allows to overcome these limitations. Finally Sect. 1.4.2.2 presents Q-Ball imaging, which can recover complex microstructures like DSI, but isn't limited by the latter's lengthy acquisition schemes.

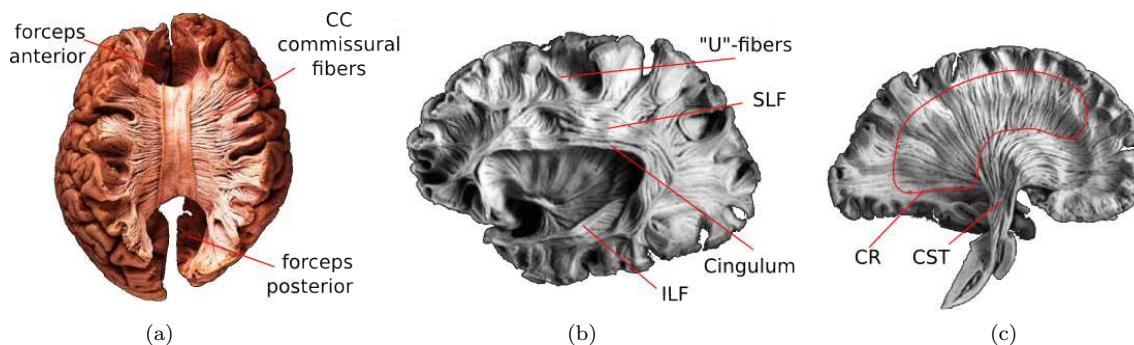


**Fig. 1.1** Major white matter fiber pathways in the brain. (a) Commissural tracts – the Corpus Callosum (CC). (b) Association tracts – short “U”-fibers connecting neighbouring gyri, the Superior Longitudinal Fasciculus (SLF), the Cingulum and the Inferior Longitudinal Fasciculus (ILF). (c) Projection tracts – the Corona Radiata (CR) and the Corticospinal Tract (CST). Adapted from [74].



151 Section 1.5 introduces briefly the computational framework consisting of sophisticated mathematical  
152 tools that have been developed for processing dMRI data and images, since these represent complex  
153 mathematical objects. In particular we present various metrics for a field of diffusion tensors in Sect.  
154 1.5.1, an algorithm that ensures that the estimated diffusion tensors are in the proper space of symmetric  
155 positive definite matrices using a Riemannian metric in Sect. 1.5.2, and a segmentation algorithm for  
156 segmenting fields or images of diffusion tensors in Sect. 1.5.3.

157 Section 1.6 is dedicated to tractography – algorithms that integrate local microstructure information to  
158 reconstruct white matter fiber pathways. Section 1.6.1 presents deterministic approaches while Sect. 1.6.2  
159 presents probabilistic approaches. The penultimate section – Sect. 1.7, is dedicated to applications. It  
160 presents the impacts of dMRI in both clinical and neuroscientific scenarios, and highlights its usefulness.

161 The chapter concludes with a summary in Sect. 1.8. In Sect. 1.9 we provide an incomplete list of  
162 important internet resources in terms of available softwares and database for processing dMRI data.

## 163 1.2 A Brief History of NMR and MRI

164 The scientific heritage of NMR and MRI is reflected in the list of Nobel laureates who contributed to  
165 their developments. The theoretical underpinnings that made NMR possible were proposed in 1924 by  
166 Wolfgang Pauli who suggested a new quantum degree of freedom that later came to be known as spin. He  
167 formulated the mathematical theory by 1927, and was awarded the Nobel prize in physics in 1945 for his  
168 contributions. The concept of spin implies that atomic nuclei bearing spins exhibit magnetic moments.  
169 The fact that protons exhibit magnetic moments had already been discovered in 1922 by Otto Stern prior  
170 to the concept of spin. Stern was awarded the Nobel prize in physics in 1943. Pauli's theory was verified  
171 in 1938 by Isidor Rabi in molecular beams. From his experiments Rabi was able to both detect the effects  
172 of spin and measure the gyromagnetic ratio that is the characteristic signature of an atomic nucleus due  
173 to its spin. His experiments also established the concept and the technique of NMR for manipulating  
174 spins. Rabi was awarded the Nobel prize in physics in 1944.

175 In 1946 Felix Bloch [12] and Edward Mills Purcell [56] independently extended the techniques estab-  
176 lished by Rabi. They successfully demonstrated the magnetic resonance effect in liquids and solids. Bloch  
177 and Purcell shared the Nobel prize of 1952 in physics, and NMR was established. In his seminal paper  
178 of 1950 [31] Erwin Hahn proposed the spin echo experiment, which used a combination of  $90^\circ$  and  $180^\circ$   
179 electromagnetic or radio frequency pulses to filter out effects of magnetic field inhomogeneities in the  
180 measurement of the transverse signal. Further works of Herman Carr and Purcell in 1954 [14] led to the  
181 full development of the radio frequency pulse technique introduced by Hahn. This formed the foundations  
182 of NMR.

183 It must be noted at this point that both the papers of Hahn [31] and Carr & Purcell [14] critically  
184 point out the observed effects of diffusion of the spin bearing nuclei in magnetic resonance experiments  
185 with a succession of radio frequency pulses. Although these papers generally perceive the diffusion effect  
186 as an unfortunate phenomenon resulting in a loss of signal, Carr & Purcell [14] in fact demonstrate that  
187 diffusion can be directly measured from NMR and go on to actually measure the diffusion constant of  
188 water at  $25^\circ\text{C}$ . This forms the corner-stone of diffusion NMR.

189 Although NMR became a well established technique for studying various materials, it took almost  
190 three decades since the experiments of Bloch and Purcell in 1946, for MRI to be invented. NMR by itself  
191 is capable of examining a single spin ensemble or a tiny region of a sample, but it can't image the whole  
192 sample to recreate a 2D slice or a 3D volumetric image necessary to study entire biological samples like  
193 the human body. Paul Lauterbur in 1973 [37] proposed the use of magnetic gradient fields to spatially  
194 encode the positions or voxel regions of the spin ensembles. This was a remarkable invention, which  
195 made it possible to reconstruct entire slice or volumetric images from NMR data. Spatial encoding was  
196 improved in terms of frequency encoding by Richard Ernst in 1978, and phase encoding by Bill Edelstein  
197 in 1980 using pulsed gradients. In 1977 Peter Mansfield [42] developed the mathematical framework for  
198 rapidly switching gradients for spatial encoding, greatly speeding up the process of reconstructing images  
199 of an entire biological sample. This is known as *echo planar imaging* (EPI). Lauterbur and Mansfield  
200 were jointly awarded the Nobel prize in medicine in 2003 for making MRI possible. Thus modern MRI  
201 was developed from the phenomenon of NMR coupled with the method of spatial encoding.

### 202 1.3 Nuclear Magnetic Resonance & Diffusion

203 The principles of NMR are based on *spin*, a fundamental quantum characteristic possessed by electrons,  
 204 protons, and neutrons, like electrical charge and mass. Spins come in multiples of  $1/2$  and can be positive  
 205 or negative. In grouped particles, e.g. atomic nuclei, opposite spin-signs can pair up to eliminate the  
 206 total spin of the group. But the net spin of unpaired particles or atomic nuclei imparts a magnetic dipole  
 207 moment. In other words such particles or such atomic nuclei can be influenced by an external magnetic  
 208 field. In the presence of a strong magnetic field  $\mathbf{B}_0$  with magnitude  $B_0$ , the magnetic dipole moment  
 209 vector or the spin vector of the particle or nucleus aligns itself with  $\mathbf{B}_0$  and precesses around it with  
 210 an angular frequency known as the *Larmor frequency*  $\omega_0 = \gamma B_0$ , where  $\gamma$  is the *gyromagnetic ratio*,  
 211 characteristic of the particle or the nucleus. The effect is detectable when it becomes pronounced in the  
 212 presence of an ample collection of spin bearing particles or nuclei with the same gyromagnetic ratio.  
 213 From a macroscopic perspective, when such a collection is subjected to a magnetic field, the randomly  
 214 oriented individual magnetic dipole moment vectors align themselves along  $\mathbf{B}_0$ . Laws of thermodynamics  
 215 ensure that a greater number of spins point along the magnetic field (low energy configuration) than  
 216 opposite to it (high energy configuration). This forms a resultant ensemble magnetic dipole moment  
 217 vector  $\mathbf{M}$ . Conventionally the external magnetic field  $\mathbf{B}_0$  is considered to be aligned with the Z-axis. The  
 218 XY-plane is then known as the transverse plane, and the net magnetization vector  $\mathbf{M}$  can be separated  
 219 into the *longitudinal* component  $\mathbf{M}_z$ , along the Z-axis (or  $\mathbf{B}_0$ ), and the *transverse* component  $\mathbf{M}_{xy}$ , in  
 220 the transverse plane (Fig. 1.2).

221 Of particular interest is the hydrogen nucleus  $^1H$ , which is found abundantly in nature, accounting for  
 222 99.98% of all hydrogen atoms, and also constituting water. 60% of the human body and 78% of the brain  
 223 is water. Therefore,  $^1H$  is a natural spin bearing nucleus of choice for MRI.  $^1H$  is an unpaired proton  
 224 with a net spin of  $1/2$ , and has a gyromagnetic ratio of  $\gamma = 42.58 \text{ MHz/T}$ .

225 The NMR signal is generated by exposing the ensemble of spins precessing along  $\mathbf{B}_0$  to an oscillating  
 226 magnetic field or an electro-magnetic (radio-frequency: RF) pulse. This is known as the excitation phase.  
 227 The energy absorbed by the low energy configuration spins from this pulse tilts the magnetization vector  
 228  $\mathbf{M}$  away from  $\mathbf{B}_0$  towards the high energy configuration. The oscillation of the secondary magnetic  
 229 field ensures that the spins (and hence  $\mathbf{M}$ ) continue to precess around  $\mathbf{B}_0$  even tilted away from it –  
 230 along the surface of a cone (Fig. 1.2). Once the RF pulse is switched off, the spins begin to recover  
 231 their alignment with the main magnetic field  $\mathbf{B}_0$ , and to return to their low energy configuration or the  
 232 thermal equilibrium. This is known as the relaxation phase. The signal is created as the spins precess  
 233 tilted away from  $\mathbf{B}_0$ , and it decays as the spins relax, dissipating the absorbed energy. The longitudinal  
 234 relaxation and the transverse relaxation of  $\mathbf{M}$  are governed by different phenomena and are characterized  
 235 by different time signatures.

236 The *longitudinal relaxation* is known as the T1 relaxation since it is described using a time signature  
 237 denoted T1. The T1 relaxation occurs as the spin ensemble radiates the energy it had absorbed from  
 238 the RF pulse to the surrounding thermal reservoir or lattice and regains its thermal equilibrium with  
 239 the lattice. Therefore, the T1 relaxation is also known as the *spin-lattice* relaxation. In this process the

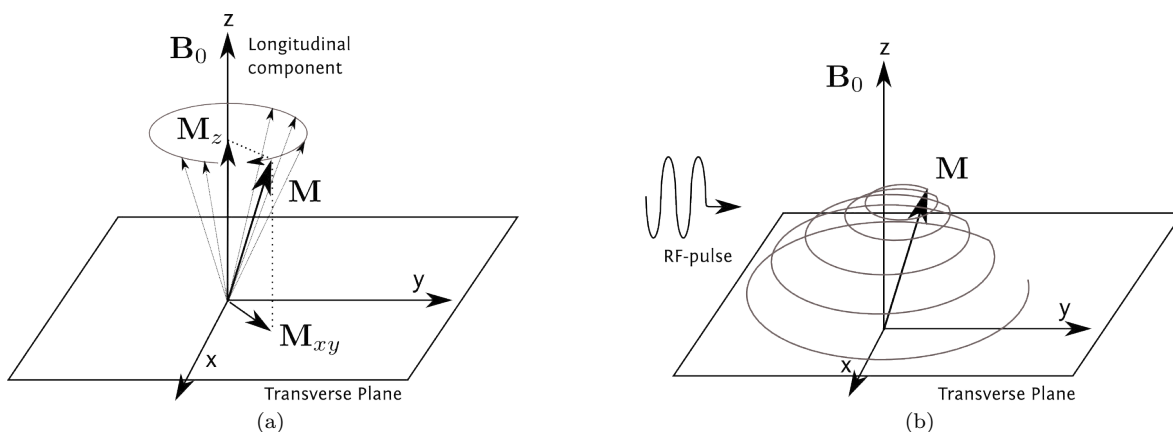


**Fig. 1.2** Nuclear Magnetic Resonance. (a) A net magnetization dipole moment vector  $\mathbf{M}$  forms when spins are exposed to an external magnetic field  $\mathbf{B}_0$ . (b) The NMR signal is generated by exciting the ensemble of spins precessing along  $\mathbf{B}_0$  by exposing them to a radio-frequency pulse – the magnetization vector  $\mathbf{M}$  spirals down to the transverse plane in the fixed frame of reference.

240 spins realign themselves with  $\mathbf{B}_0$ . In terms of the net magnetization vector  $\mathbf{M}$ , this implies that the  
 241 longitudinal component  $M_z$  progressively regains its initial magnitude, while the transverse component  
 242  $M_{xy}$  progressively becomes null again.

243 The *transverse relaxation* involves the phenomenon of the spins regaining their thermal equilibrium  
 244 amongst themselves, and is characterized by the time signature T2. Therefore it is also known as the  
 245 *spin-spin* relaxation or the T2 relaxation. In the transverse plane this is interpreted by the spins losing  
 246 their initial coherence. From an initial coherent transverse magnetization vector  $\mathbf{M}_{xy}$ , they progressively  
 247 dephase as they radiate the energy they had absorbed to neighbouring spins. Transverse relaxation is,  
 248 however, a complex phenomenon. Although theoretically  $\mathbf{B}_0$  is supposed homogeneous, in reality minor  
 249 inhomogeneities exist. These inhomogeneities are relevant enough to also contribute to spins dephasing in  
 250 the transverse plane, though this is not a true relaxation. Transverse relaxation is therefore a combination  
 251 of spin-spin relaxation and field inhomogeneity dephasing. The pure spin-spin relaxation time is known  
 252 as T2. The combined transverse relaxation time is known as T2\*.

253 The *Bloch equations* are a coupled set of three differential equations that combine the effects of NMR  
 254 and describe the evolution of the net magnetization vector  $\mathbf{M}$  over time. These are macroscopic and  
 255 phenomenological equations that include the effects of Larmor precession and T1 and T2 relaxations.  
 256 They are written in the fixed frame of reference in terms of the relaxation time constants as:

$$\frac{d\mathbf{M}(t)}{dt} = \gamma\mathbf{M}(t) \times \mathbf{B}(t) + \begin{pmatrix} -\frac{1}{T_2} & 0 & 0 \\ 0 & -\frac{1}{T_2} & 0 \\ 0 & 0 & -\frac{1}{T_1} \end{pmatrix} \mathbf{M}(t) + \begin{pmatrix} 0 \\ 0 \\ \frac{M_0}{T_1} \end{pmatrix}, \quad (1.1)$$

257 where  $\mathbf{B}(t)$  is the total external magnetic field.

### 258 1.3.1 The Hahn Spin Echo Experiment

259 Erwin L Hahn was the first to notice the effects of diffusion when he conceived the *spin echo* experiment  
 260 to remove the effects of field inhomogeneities or T2\* from the signal [31]. Diffusion NMR is derived from  
 261 Hahn's original spin echo experiment of 1950. Hahn put forth the idea that following a  $90^\circ$  RF pulse that  
 262 tilts the net magnetization vector to the transverse plane, the dephasing that follows caused by the field  
 263 inhomogeneities, could be refocused using a second RF pulse of  $180^\circ$ , thus removing the effects of the  
 264 field inhomogeneities.

265 After the  $90^\circ$  RF pulse, the spins precessing in the transverse plane should appear static in a frame of  
 266 reference rotating at the Larmor frequency. However, due to field inhomogeneities, as the spins begin to

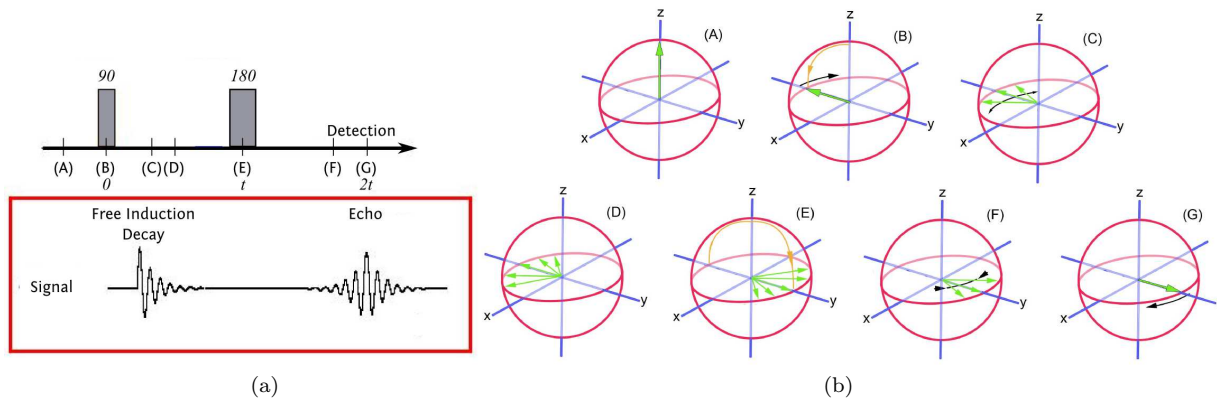


**Fig. 1.3** The Hahn Spin Echo experiment. (a) Pulse sequence with Free Induction Decay & signal echo. Adapted from Wikipedia. (b) Concept of spin echo refocusing in the rotating frame of reference. (A) The net magnetization vector  $\mathbf{M}$  (green vector), initially aligned with the Z-axis under the influence of  $\mathbf{B}_0$ . (B)  $90^\circ$  RF pulse tilts (orange arrow)  $\mathbf{M}$  on to the transverse plane. (C) & (D) Spins dephasing due to local field inhomogeneities. Slow spins fall back, while the fast spins move ahead in the transverse plane. (E)  $180^\circ$  RF pulse (orange arrow) flips the spins around such that now the slow spins are ahead and the fast spins are behind. (F) Refocussing begins as the fast spins begin to catch up the slow spins from behind. The echo begins to form. (G) The spins are completely refocused. This is the centre of the echo and the signal is free of the effects of field inhomogeneities. Drawing by A.G. Filler, image source Wikipedia.

dephase, some would appear to speed up (or move ahead clockwise in the rotating frame of reference), while some would slow down (or fall back anti-clockwise in the rotating frame of reference). This transverse dephasing is known as the *free induction decay* (FID) and causes the signal to decay faster than pure T2 effects. However the application of a second RF pulse of  $180^\circ$  has the effect of flipping the individual spins in the transverse plane such that the “slow” spins that had fallen behind the rotating frame of reference are flipped ahead of it, while the “fast” spins that had moved ahead are flipped behind the rotating frame of reference. Indeed, the  $180^\circ$  RF pulse causes the spins to refocus after a certain length of time as the fast spins catch up with the slow spins, which regenerates the signal. This is known as the *echo* and it is free of the T2\* effects due to field inhomogeneities (Fig. 1.3).

It must be noted, however, that the echo regenerates the signal completely only under the assumption that none of the spins in the ensemble have moved. If they move then the  $180^\circ$  RF pulse doesn’t completely invert the spin and this results again in signal decay. However, this is not due to field inhomogeneities. As noted by Hahn [31] and Carr & Purcell [14], this is due to the translational motion of diffusion. This forms the basis of diffusion NMR.

### 1.3.2 Diffusion

Diffusion NMR (dNMR) is a modality of NMR that is sensitive to the Brownian motion of the particles in a sample. The dNMR experiment can therefore be used to measure the diffusion properties of the underlying sample. This makes dNMR central to diffusion MRI. At the heart of dNMR is the diffusion process, and understanding diffusion helps to understand how it can be measured from NMR. It leads to the critical improvements that were made by Stejskal & Tanner to the original spin echo experiments of Hahn and Carr & Purcell that opened up the domain of dNMR.

Diffusion is a process of mass transport that describes the random spreading of molecules or particles generally in the presence of a concentration gradient. The process of diffusion was observed, studied and mathematically described over the entire 19th century. It was initially observed in three different forms, namely heat diffusion in the presence of a temperature gradient, molecular diffusion in the presence of a concentration gradient, and Brownian motion, which occurs even in the absence of any gradients. These, apparently very different phenomena – the first, concerning the spreading of energy in a solid medium, the second, concerning the spreading of molecules from a region of high concentration to a region of low concentration in fluids, and the third, concerning the random motion of molecules and particles in fluids due to the ambient temperature – can all be described by the same diffusion equation. However, while today their correspondence is widely accepted, establishing this connection wasn’t always an easily demonstrable task.

**Fick’s Laws of Diffusion:** The phenomenological equations of diffusion were proposed by Joseph Fourier in 1822 to describe the diffusion of heat in solids, and then adapted by Adolf Fick in 1855 to describe the diffusion of molecules in fluids in the presence of a concentration gradient [21]. Fick derived his “laws of diffusion” from Fourier’s laws by analogy, while attempting to describe the experiments conducted by Thomas Graham in 1831 on the diffusion of gases. These laws describe the molecular transfer or diffusion that takes place in a system from regions of high concentration to regions of low concentration due to the concentration gradient.

Fick’s first law relates the rate of transfer of the diffusing substance per unit area, or flux  $\mathbf{J}$ , to the concentration gradient  $\mathbf{C}$  causing the diffusion:

$$\mathbf{J} = -D\nabla\mathbf{C}, \quad (1.2)$$

where  $D$  is the diffusion coefficient. Conservation of mass during the diffusion process implies  $-\nabla\mathbf{J} = \partial\mathbf{C}/\partial t$ . This leads to Fick’s second law of diffusion:

$$\frac{\partial\mathbf{C}}{\partial t} = D\nabla^2\mathbf{C}. \quad (1.3)$$

Fick’s second law describes the change of the concentration field over time due to the diffusion process. Eq. (1.3), which relates the time derivative of the concentration to the second order spatial derivative of the concentration is known as the *diffusion equation* – it describes diffusion phenomenologically.

$D$  being a scalar quantity in Eqs. (1.2 – 1.3) is an indication that diffusion is equal in all directions. This is known as *isotropic* diffusion. However, certain media such as crystals, textile fibers, etc. can be

315 inherently anisotropic and can favour diffusion in a certain spatial direction while hindering it in others.  
 316 This results in *anisotropic* diffusion, which is described by replacing the scalar diffusion coefficient  $D$  by  
 317 a generalized *diffusion tensor*  $\mathbf{D}$  ( $3 \times 3$  matrix) in Fick's laws [21]:

$$\mathbf{J} = -\mathbf{D}\nabla\mathbf{C}, \quad (1.4)$$

$$\frac{\partial\mathbf{C}}{\partial t} = \nabla \cdot (\mathbf{D}\nabla\mathbf{C}). \quad (1.5)$$

318 Diagonalizing the diffusion tensor  $\mathbf{D}$  into its eigenvalues and eigenvectors provides a local orthogonal  
 319 coordinate system that indicates the preferential diffusion direction favoured by the anisotropy of the  
 320 underlying material. This is the budding idea that indicates that diffusion can be considered as a probe  
 321 of the underlying medium's microstructure. Isotropic diffusion can be understood as a special case of  
 322 anisotropic diffusion when  $\mathbf{D} = D\mathbf{I}$ , where  $\mathbf{I}$  is the identity matrix. The idea of the diffusion tensor is  
 323 central to dMRI, since the fibrous quality of the cerebral white matter also exhibits directional anisotropy.

324 **Brownian Motion & Einstein's Random Walk Approach:** Although Fick's laws are concerned  
 325 with the diffusion of molecules from regions of high concentration to regions of low concentration, they  
 326 essentially describe the evolution of the concentration gradient over time and space, and aren't concerned  
 327 with the movements of the molecules themselves. The molecular description of diffusion emerged with  
 328 Albert Einstein in 1905 when he related the molecular-kinetic theory of heat to the observations made  
 329 by Robert Brown in 1828. Brown had noted the perpetual erratic motion of pollen grains suspended  
 330 in water while observing them under a microscope. This erratic movement came to be known by his  
 331 name as Brownian motion. When Einstein proposed [28] that due to the thermal kinetic energy of  
 332 molecules, particles suspended in a liquid large enough to be observed under a microscope would exhibit  
 333 random movements governed by the probabilistic law he derived, his idea was quickly recognized to be  
 334 the theoretical description of Brownian motion. It turned out that the probabilistic law of Brownian  
 335 motion derived by Einstein also satisfied the diffusion equation. This provided the final link and showed  
 336 that diffusion was driven by the thermal kinetic energy of molecules due to the ambient temperature,  
 337 implying that diffusion, in the form of Brownian motion also occurred in the absence of a temperature or  
 338 a concentration gradient. The special case of diffusion when the suspended particles belong to the liquid  
 339 is known as *self diffusion*.

340 To describe the erratic movement of a large number of particles undergoing Brownian motion, Einstein  
 341 adopted the probabilistic approach of a random walk model [28]. He modelled diffusion using two Proba-  
 342 bility Density Functions (PDF)s -  $f(\mathbf{x}, t)$ , the probability of finding a particle at the position  $\mathbf{x}$  at a time  $t$ ,  
 343 and  $P(\Delta\mathbf{x}, \Delta t)$ , the transition probability or the probability of finding a particle at a distance  $\Delta\mathbf{x}$  from its  
 344 initial position after a time  $\Delta t$ . Considering  $P(\Delta\mathbf{x}, \Delta t)$  symmetric, such that  $P(\Delta\mathbf{x}, \Delta t) = P(-\Delta\mathbf{x}, \Delta t)$ ,  
 345 Einstein proposed the relation between  $f(\mathbf{x}, t)$  and  $P(\Delta\mathbf{x}, \Delta t)$ :

$$f(\mathbf{x}, t + \Delta t) = \int_{-\infty}^{\infty} f(\mathbf{x} - \Delta\mathbf{x}, t)P(\Delta\mathbf{x}, \Delta t)d\Delta\mathbf{x}. \quad (1.6)$$

346 He then showed that  $f(\mathbf{x}, t)$ , which can also be considered as the local particle concentration, satisfies  
 347 the diffusion equation:

$$\frac{\partial f(\mathbf{x}, t)}{\partial t} = D\nabla^2 f(\mathbf{x}, t), \quad (1.7)$$

348 which introduces the diffusion coefficient  $D$ , showing that the random walk approach can model dif-  
 349 fusion. In the isotropic case discussed by Einstein, he further showed that the diffusion coefficient is  
 350 directly proportional to the variance of the particle displacement  $\langle(\Delta x)^2\rangle = 2\Delta tD$ , where without loss  
 351 of generality  $x$  is any chosen spatial direction. A similar development in the anisotropic case along the  
 352 lines proposed by Einstein results in the anisotropic diffusion equation and connects the diffusion tensor  
 353 to the covariance tensor:

$$\frac{\partial f(\mathbf{x}, t)}{\partial t} = \nabla \cdot (\mathbf{D}\nabla f(\mathbf{x}, t)), \quad (1.8)$$

$$\mathbf{D} := \frac{1}{2\Delta t} \begin{pmatrix} \langle(\Delta x)^2\rangle & \langle\Delta x\Delta y\rangle & \langle\Delta x\Delta z\rangle \\ \langle\Delta y\Delta x\rangle & \langle(\Delta y)^2\rangle & \langle\Delta y\Delta z\rangle \\ \langle\Delta z\Delta x\rangle & \langle\Delta z\Delta y\rangle & \langle(\Delta z)^2\rangle \end{pmatrix}. \quad (1.9)$$

354 Finally Einstein also derived that under the initial condition  $f(\mathbf{x}, 0) = \delta(\mathbf{x})$ , which corresponds to free  
 355 diffusion, the local particle concentration  $f(\mathbf{x}, t)$  is a Gaussian function with the derived variance  $2tD$ .

356 This, however, implies that the Green's function of the diffusion equation, or the transition probability  
 357 is also a Gaussian in the case of free diffusion:

$$P(\Delta\mathbf{x}, \Delta t) = \frac{1}{(4\pi\Delta t)^{3/2}|\mathbf{D}|^{1/2}} \exp\left(-\frac{\Delta\mathbf{x}^T\mathbf{D}^{-1}\Delta\mathbf{x}}{4\Delta t}\right). \quad (1.10)$$

358 In the anisotropic case it is an oriented Gaussian parameterized by the covariance tensor.

### 359 1.3.3 The Stejskal-Tanner PGSE Experiment

360 After Hahn who first noticed the effects of diffusion in NMR in his spin echo experiment [31], Carr &  
 361 Purcell measured the diffusion coefficient for the first time from NMR. In their modification to Hahn's  
 362 experiment they employed a temporally constant magnetic gradient field and modelled the diffusion  
 363 of spin bearing particles with discrete jumps [14]. However, the continuous description was formulated  
 364 by Torrey in 1956. He modified the phenomenological Bloch equations by adding to it Fick's diffusion  
 365 equation (Eq. 1.3) [64]. This came to be known as the Bloch-Torrey equation for describing the net  
 366 magnetization vector  $\mathbf{M}$  (without flow):

$$\frac{\partial\mathbf{M}}{\partial t} = \gamma\mathbf{M} \times \mathbf{B} + \begin{pmatrix} -\frac{1}{T_2} & 0 & 0 \\ 0 & -\frac{1}{T_2} & 0 \\ 0 & 0 & -\frac{1}{T_1} \end{pmatrix} \mathbf{M} + \begin{pmatrix} 0 \\ 0 \\ \frac{M_0}{T_1} \end{pmatrix} + D\nabla^2\mathbf{M}, \quad (1.11)$$

367 where Fick's law is employed to describe the self diffusion of the net magnetization.

368 About a decade later, in 1965, Stejskal & Tanner designed the *pulsed gradient spin echo* (PGSE)  
 369 experiment by modifying Hahn's spin echo experiment with two identical magnetic gradients around the  
 370  $180^\circ$  RF pulse to encode the transverse phase of the diffusing spin bearing particles [62, 61] (Fig. 1.4).  
 371 This made it easier to measure the decay in the transverse signal due to diffusion, and from there the  
 372 diffusion coefficient. The PGSE experiment established the field of dNMR.

373 In the PGSE experiment the first gradient  $\mathbf{G}$  of duration  $\delta$  spatially encodes the phase of the individual  
 374 spins (by dephasing them by an amount dependent on their position), and the effects of this gradient are  
 375 undone by the second identical gradient after the  $180^\circ$  RF pulse which flips the spins around (implying  
 376 an effect  $-\mathbf{G}$  from the second gradient). This results in a complete recovery of the signal since the  
 377 magnitude of transverse magnetization vector  $\mathbf{M}_{xy}$  depends on the phase coherence of the individual  
 378 spins. However, if the individual spins move due to diffusion during the period  $\Delta$ , between the two pulsed  
 379 gradients, then the effects of the second gradient isn't the exact opposite of the first gradient ( $-\mathbf{G}$ )  
 380 that was used to encode their phases. This leads to a partial phase incoherence – resulting in a reduced  
 381 transverse magnetization  $\mathbf{M}_{xy}$ , implying a loss in the spin echo signal. Since the signal decay is related to  
 382 the rate of diffusion or the diffusion coefficient, measuring the signal decay makes it possible to measure  
 383 the diffusion coefficient.

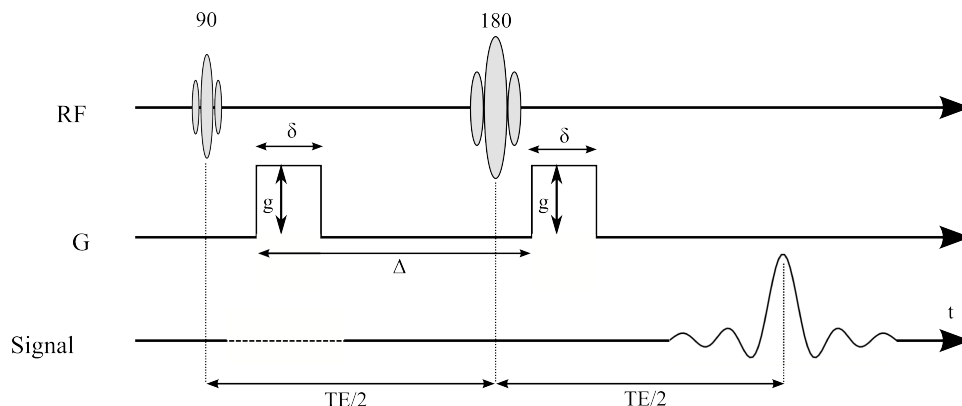


**Fig. 1.4** The pulsed gradient spin echo (PGSE) sequence. Two identical gradients are applied around the  $180^\circ$  RF pulse of Hahn's spin echo experiment. This encodes the transverse phase of the diffusing spin bearing particles. It then becomes easier to measure the decay of the signal due to diffusion.

384 Stejskal and Tanner provided the mathematical solution to the Bloch-Torrey differential equation  
 385 for their PGSE experiment, which became the corner stone equation for dNMR as the Stejskal-Tanner  
 386 equation for the signal:

$$S = S_0 \exp \left( -\gamma^2 \delta^2 g^2 \left( \Delta - \frac{\delta}{3} \right) D \right) = S_0 \exp(-bD), \quad (1.12)$$

387 where  $S$  is the magnitude of the signal decay due to diffusion,  $S_0$  is the magnitude of the signal in the  
 388 absence of a diffusion encoding gradient,  $\Delta$  is the time between the two gradients,  $\delta$  is the application  
 389 time of each gradient, and  $b = \gamma^2 \delta^2 g^2 \left( \Delta - \frac{\delta}{3} \right)$  is the b-value. The modifications introduced by Stejskal  
 390 and Tanner in the PGSE experiment, therefore, makes it possible to measure the diffusion coefficient  $D$   
 391 a regular spin-echo experiment in NMR.

392 In the same year, Stejskal further considered diffusion in anisotropic media by employing the anisotropic  
 393 Fick's law (Eq. 1.5) instead of the isotropic law (Eq. 1.3), in the Bloch-Torrey equation, which introduces  
 394 the diffusion tensor  $\mathbf{D}$  [61]. He was able to derive the modified Stejskal-Tanner equation incorporating  
 395 the diffusion tensor in anisotropic media [61]:

$$S = S_0 \exp \left( -\gamma^2 \delta^2 g^2 \left( \Delta - \frac{\delta}{3} \right) \mathbf{g}^T \mathbf{D} \mathbf{g} \right) = S_0 \exp(-b\mathbf{g}^T \mathbf{D} \mathbf{g}). \quad (1.13)$$

396 However, Stejskal in this seminal paper fell short of providing a method for measuring the diffusion tensor  
 397 from NMR, which could have preempted diffusion tensor imaging by almost three decades. But he did  
 398 lay the foundations of the q-space formalism with the ‘‘pulsed’’ gradient assumption.

### 399 1.3.4 Narrow Gradient Pulse PGSE: q-space Formalism

400 Diffusion in the PGSE experiment can also be modelled from a probabilistic or random-walk model  
 401 driven by the thermal kinetic energy of the spin bearing particles. The PGSE experiment (Fig. 1.4)  
 402 spatially encodes or labels the transverse phase of the spins using the first gradient, which results in a  
 403 deliberate dephasing of the transverse magnetization. The purpose of the second gradient after the 180°  
 404 RF pulse is to undo the effects of the first gradient and rephase the transverse magnetization. However, if  
 405 the spins diffuse away from their position between the two gradients, then the transverse magnetization  
 406 isn't entirely rephased after the second gradient, resulting in a loss of the transverse signal. This can be  
 407 described by using a random-walk approach for the spin bearing particles.

408 Under the assumption  $\delta \ll \Delta$ , which is known as the *narrow gradient pulse* (NGP) condition, which  
 409 implies that the spins are static during the application of the diffusion encoding gradients  $\mathbf{G}(t)$ , the  
 410 dephasing accrued by a spin in the initial position  $\mathbf{r}_0$  during the first gradient is [44]  $\phi_1 = \gamma \int_0^\delta \mathbf{G}(t) \cdot \mathbf{r}_0 dt =$   
 411  $\gamma \delta \mathbf{G} \cdot \mathbf{r}_0$ , when  $\mathbf{G}(t) = \mathbf{G} = g\mathbf{g}$ . Similarly the dephasing accrued by the spin, now in the position  $\mathbf{r}$  due  
 412 to diffusion, during the second gradient is  $\phi_2 = \gamma \int_{\Delta}^{\Delta+\delta} \mathbf{G}(t) \cdot \mathbf{r} dt = \gamma \delta \mathbf{G} \cdot \mathbf{r}$ . Since the second gradient  
 413 is applied after the 180° RF pulse, which flips the spins around, the net phase shift accrued by a spin is  
 414  $\phi = \phi_2 - \phi_1 = \gamma \delta \mathbf{G} \cdot (\mathbf{r} - \mathbf{r}_0)$ . Of course, if the spins hadn't diffused and had remained static during the  
 415 period  $\Delta$  (between the gradients), then the net phase shift would have cancelled out. In other words the  
 416 amount of net phase shift is proportional to the diffused distance  $(\mathbf{r} - \mathbf{r}_0)$ .

417 The NGP condition  $\delta \ll \Delta$  can also be interpreted in the way Stejskal proposed it  $\delta \rightarrow 0$ , with  $\delta \mathbf{G}$   
 418 finite. Although in practice the NGP condition can never be achieved, it provides a powerful insight into  
 419 the process of measuring diffusion from NMR.

420 The complex signal generated by individual spins with a net phase shift  $\phi$  is  $\exp(i\phi) = \exp[i\gamma \delta \mathbf{G} \cdot (\mathbf{r} - \mathbf{r}_0)]$   
 421 [13, 44]. However, the spin echo signal  $E(\mathbf{G}, \Delta)$  is the averaged net signal from the spin ensemble, or it is  
 422 the expected value of the complex signal given the probability of spins starting at  $\mathbf{r}_0$  and diffusing to  $\mathbf{r}$  in  
 423 the time  $\Delta$ . This probability is the product of the probabilities  $f(\mathbf{r}_0, 0)$ , of finding a spin initially at  $\mathbf{r}_0$ ,  
 424 and  $P(\mathbf{r}|\mathbf{r}_0, \Delta)$ , of a single spin starting at  $\mathbf{r}_0$  and diffusing to  $\mathbf{r}$  in time  $\Delta$ . The product  $f(\mathbf{r}_0, 0)P(\mathbf{r}|\mathbf{r}_0, \Delta)$   
 425 introduces the random-walk model for the spin bearing particles diffusing from  $\mathbf{r}_0$  to  $\mathbf{r}$ , and [13]:

$$E(\mathbf{G}, \Delta) = \int f(\mathbf{r}_0, 0) \int \exp[i\gamma \delta \mathbf{G} \cdot (\mathbf{r} - \mathbf{r}_0)] P(\mathbf{r}|\mathbf{r}_0, \Delta) d\mathbf{r} d\mathbf{r}_0. \quad (1.14)$$

426 This indicates that in the absence of diffusion encoding gradients  $E(\mathbf{0}, t) = 1$ . In practice  $E(\mathbf{G}, \Delta)$  is  
 427 obtained by dividing the echo signal amplitude from a PGSE experiment with diffusion gradients by the  
 428 echo signal amplitude from a Hahn spin echo experiment without gradients  $E(\mathbf{G}, \Delta) = S(\mathbf{G})/S_0$ .

429 This leads to the q-space formalism by defining a reciprocal space  $\mathbf{q}$  where [13]  $\mathbf{q} := \gamma\delta\mathbf{G}/2\pi$ . Inserting  
 430  $\mathbf{q}$  in Eq. (1.14) gives the q-space signal:

$$E(\mathbf{q}, \Delta) = \int f(\mathbf{r}_0, 0) \int \exp[i2\pi\mathbf{q} \cdot (\mathbf{r} - \mathbf{r}_0)] P(\mathbf{r}|\mathbf{r}_0, \Delta) d\mathbf{r} d\mathbf{r}_0. \quad (1.15)$$

431 Assuming the transition probability  $P(\mathbf{r}|\mathbf{r}_0, \Delta)$  to be translationally invariant or that the movement of  
 432 a spin is independent of the movements of the other spins and also of its own position and movements in  
 433 the past – as in a random-walk, implies that  $P(\mathbf{r}|\mathbf{r}_0, \Delta) = P(\Delta\mathbf{r}, \Delta)$ , which is the diffusion propagator.  
 434 Also since in a random-walk the movements of all the particles are independent and identical, and since the  
 435 complex signal and the diffusion propagator for a spin only depend on the spin displacement  $\Delta\mathbf{r} = (\mathbf{r} - \mathbf{r}_0)$ ,  
 436 it is useful to consider the *ensemble average propagator* (EAP), which describes the average probability  
 437 of any spin in the ensemble diffusing by  $\Delta\mathbf{r}$  during the time  $\Delta t$  [13]:

$$\bar{P}(\Delta\mathbf{r}, \Delta t) = \int P(\Delta\mathbf{r}, \Delta t) f(\mathbf{r}_0, 0) d\mathbf{r}_0. \quad (1.16)$$

438 Combining Eqs. (1.15 – 1.16) gives the main result of the q-space formalism [13]:

$$E(\mathbf{q}, t) = \int \bar{P}(\Delta\mathbf{r}, t) \exp(i2\pi\mathbf{q} \cdot \Delta\mathbf{r}) d\Delta\mathbf{r}, \quad (1.17)$$

439 which establishes an inverse Fourier Transform relationship between the EAP, henceforth denoted  $P(\mathbf{r})$ ,  
 440 and the normalized echo signal, henceforth denoted  $E(\mathbf{q})$ .

441 This Fourier relationship between the ensemble average diffusion propagator and the diffusion NMR  
 442 signal ushers in the paradigm change that diffusion can be viewed more than just an intrinsic property,  
 443 but also as a probe of the microstructure of the underlying medium. This becomes apparent when the  
 444 medium is anisotropic and has a complex microstructure, which is the case in cerebral white matter where  
 445 numerous fiber bundles criss-cross at a resolution much finer than that of dMRI.

## 446 1.4 From Diffusion MRI to Tissue Microstructure

447 Although Stejskal in Eq. (1.13) formulated the signal for anisotropic diffusion using a *diffusion tensor*  
 448 (DT), the reason he fell short of providing a method for estimating the DT is perhaps because he was  
 449 involved with dNMR. In such experiments it was generally possible to re-orient the experimental setup  
 450 to align the primary anisotropy direction with the laboratory frame, sufficing it to measure the diffusion  
 451 coefficient in only three directions [34].

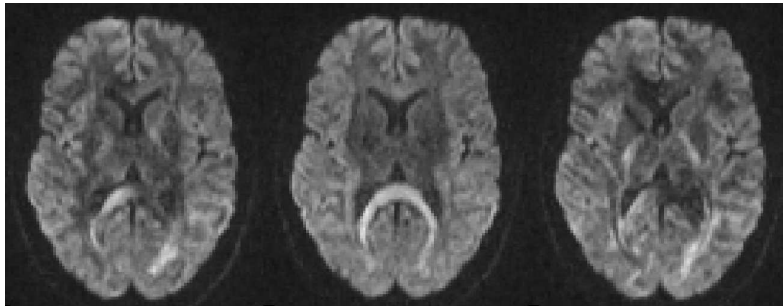


**Fig. 1.5** Diffusion Weighted Images of the brain acquired along different gradient encoding directions showing different contrasts.

452 This however changed with MRI and dMRI, when large anisotropic specimen that couldn't be rotated  
 453 in the scanner began to be imaged. Imaging such specimen, e.g. cerebral white matter tissue, or the entire  
 454 brain, revealed that the diffusion coefficient measured in such specimen depended upon the direction of the



diffusion encoding gradient. In other words the dMRI signal decay was different along different gradient directions; or again such dMRI images revealed different contrasts as the diffusion encoding gradient was rotated. These dMRI images were called Diffusion Weighted Images (DWIs). DWIs were at first cryptic because while they revealed the diffusion coefficient, they clearly also indicated that the underlying tissue was highly anisotropic, but they did not provide a method for inferring the preferential directions of this anisotropy. The diffusion coefficients computed from these DWIs using Stejskal-Tanner's isotropic signal decay formulation  $S = S_0 \exp(-bD)$  (Eq. 1.12) were called the *apparent diffusion coefficient* (ADC), since these changed in the highly anisotropic tissue depending on the direction of the diffusion encoding gradient (Fig. 1.5). This limitation of the DWI's, and of Stejskal-Tanner's isotropic signal formulation, shifted the interest from measuring only the diffusion coefficient to inferring the preferential diffusion anisotropy directions, or to using diffusion as a probe to infer the tissue's microstructure. This brought forth a whole new meaning to Stejskal's DT formulation, and it's measurement from dMRI, since its diagonalisation provided a local coordinate system that was a good indicator of the preferential diffusion anisotropy directions or the underlying medium's microstructure.

### 1.4.1 Diffusion Tensor Imaging: The Simplest Model

Diffusion tensor imaging (DTI) was introduced by Basser et al. [5, 6] in 1994, which for the first time provided a method for measuring the DT from dMRI and for inferring the local tissue microstructure from the DT. Starting from Stejskal's equation, Basser et al. defined the  $\mathbf{b}$ -matrix, which also accounted for the imaging gradients in addition to the pure diffusion encoding gradients [5, 6]. They formulated the PGSE echo signal to be:

$$S = S_0 \exp(-tr(\mathbf{bD})), \quad (1.18)$$

where  $tr(\mathbf{A})$  represents the trace of the matrix  $\mathbf{A}$ . This simplifies to Stejskal's formulation (Eq. 1.13)  $S = S_0 \exp(-b\mathbf{g}^T \mathbf{D} \mathbf{g})$  in the absence of the imaging gradients, or under the consideration that the imaging gradients are small compared to the diffusion encoding gradients, which is mostly true. Otherwise, the  $\mathbf{b}$ -matrix has to be computed from the dynamics of the imaging and the diffusion encoding gradients.

**DTI Estimation:**  $\mathbf{D}$  is a covariance tensor, therefore, it is symmetric and positive definite. This implies that there are six unknowns to be estimated from the DTI signal in Eq. (1.18). Therefore, at least six DWIs, acquired along linearly independent and non-coplanar gradient directions, and a non diffusion weighted or Hahn spin echo ( $S_0$ ) image is required to measure the six unknown coefficients of  $\mathbf{D}$ . The linearized version of Eq. (1.18) provides the simplest scheme for doing this [5, 6]:

$$\ln\left(\frac{S}{S_0}\right) = -b_{ij}D_{ij}. \quad (1.19)$$

In practice, often more than six DWIs are used to account for acquisition noise. In the case of  $N$  DWIs, the linearized equation for the signal is written in a matrix form:

$$\begin{bmatrix} -\ln(S_1/S_0) \\ -\ln(S_2/S_0) \\ -\ln(S_3/S_0) \\ \vdots \\ -\ln(S_N/S_0) \end{bmatrix} = \begin{bmatrix} b_{11}^1 & 2b_{12}^1 & 2b_{13}^1 & b_{22}^1 & 2b_{23}^1 & b_{33}^1 \\ b_{11}^2 & 2b_{12}^2 & 2b_{13}^2 & b_{22}^2 & 2b_{23}^2 & b_{33}^2 \\ b_{11}^3 & 2b_{12}^3 & 2b_{13}^3 & b_{22}^3 & 2b_{23}^3 & b_{33}^3 \\ \vdots & \vdots & \vdots & \vdots & \vdots & \vdots \\ b_{11}^N & 2b_{12}^N & 2b_{13}^N & b_{22}^N & 2b_{23}^N & b_{33}^N \end{bmatrix} \begin{bmatrix} D_{11} \\ D_{12} \\ D_{13} \\ D_{22} \\ D_{23} \\ D_{33} \end{bmatrix}, \quad (1.20)$$

$$\mathbf{X} = \mathbf{Bd}. \quad (1.21)$$

The easiest option for solving this is to use the least squares optimization  $\mathbf{d}_{opt} = argmin_{\mathbf{d}} \|\mathbf{X} - \mathbf{Bd}\|^2$ , which translates to the Moore-Penrose pseudo-inverse solution:

$$\mathbf{d} = (\mathbf{B}^T \mathbf{B})^{-1} \mathbf{B}^T \mathbf{X}.$$

Due to its linear form which only involves matrix manipulations, this solution is extremely rapid. However, it doesn't account for the signal noise or of the distortion to the noise it introduces while taking the logarithms of the signal in the linearization process. Due to DTI's popularity and maturity as a technique of probing tissue microstructures, a number of sophisticated solutions exist for measuring  $\mathbf{D}$  from the

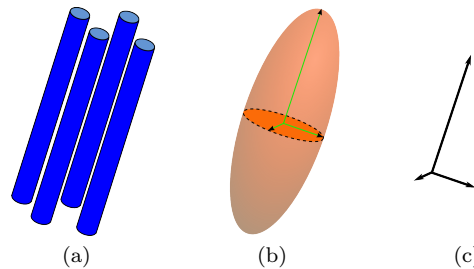


**Fig. 1.6** Microstructure from DTI. Coherent fibers (a) can be inferred from the ellipsoid of the diffusion tensor (DT) (b). The DT also provides a local coordinate system (c) that indicates the preferential diffusion anisotropy directions.

dMRI signal. These range from Bassler's original weighted least squares approach [5] which accounts for the logarithmic distortion of the signal noise, to non-linear optimization approaches that account for signal noise, spatial smoothing, and also for constraining the DT to be positive definite [18, 19, 70, 29, 45, 51, 40].

**Microstructure from DTI:** The consistency between the phenomenological approach and the q-space formalism, under the NGP condition, implies that the propagator describing the diffusion measured by DTI is the Gaussian PDF (Eq. 1.10). This is an oriented Gaussian parameterized by the DT  $\mathbf{D}$ , or its inverse. The orientation of the PDF can be deduced from the eigen-decomposition of the DT. The eigenvalues and eigenvectors of  $\mathbf{D}$  form a local coordinate system that indicates the preferential diffusion direction orienting the Gaussian PDF. In other words it indicates the diffusion direction favoured by the microstructure of the medium. This preferential orientation of the microstructure can be visually represented by the ellipsoid represented by  $\mathbf{D}$  whose implicit quadratic form is [6]:

$$\frac{\mathbf{x}^T \mathbf{D}^{-1} \mathbf{x}}{2t} = 1. \quad (1.22)$$

Since  $\mathbf{D}$  is symmetric it can be diagonalized  $\mathbf{D} = \mathbf{W}^T \mathbf{\Lambda} \mathbf{W}$ , where  $\mathbf{W}$  are its orthonormal eigenvectors and  $\mathbf{\Lambda}$  is a diagonal matrix whose diagonal elements are its eigenvalues. The canonical form of the diffusion ellipsoid defined by  $\mathbf{D}^{-1}$  emerges in the coordinate frame of its eigenvectors:

$$\left( \frac{x'}{\sqrt{2\lambda_1 t}} \right)^2 + \left( \frac{y'}{\sqrt{2\lambda_2 t}} \right)^2 + \left( \frac{z'}{\sqrt{2\lambda_3 t}} \right)^2 = 1.$$

To infer the microstructure of the cerebral white matter from DTI, the fundamental assumption is that the coherent fiber bundle structures formed by the axons hinder the perpendicular diffusion of water molecules (spin bearing  $^1H$  atoms) more than the parallel diffusion. Therefore, the elongation and orientation of the DT are good indicators of these coherent structures or fiber bundles locally. The eigenvector corresponding to the largest eigenvalue, the major eigenvector, indicates the main fiber direction, while the other eigenvectors and eigenvalues indicate diffusion anisotropy in the perpendicular plane (Fig. 1.7).

**Scalar Measures:** The microstructure of the medium or the white matter can be further characterized from a number of rotationally invariant scalar measures derived from the DT that reveal diffusive properties of the underlying tissue. A number of such scalar measures are of primary importance since they are often used as bio-markers.

- The first is *mean diffusivity* (MD) [4]:

$$\bar{\lambda} = \text{tr}(\mathbf{D})/3.$$

- *Fractional anisotropy* (FA) is the other measure which describes the amount of anisotropy presented by the microstructure. It too is derived from the eigenvalues of  $\mathbf{D}$  ( $\lambda_1 \geq \lambda_2 \geq \lambda_3$ ) [4]:

$$\text{FA} = \sqrt{\frac{3}{2}} \sqrt{\frac{(\lambda_1 - \bar{\lambda})^2 + (\lambda_2 - \bar{\lambda})^2 + (\lambda_3 - \bar{\lambda})^2}{\lambda_1^2 + \lambda_2^2 + \lambda_3^2}},$$

- The *Relative anisotropy* (RA) is given by [4]:

$$\text{RA} = \frac{1}{\sqrt{3}} \sqrt{\frac{(\lambda_1 - \bar{\lambda})^2 + (\lambda_2 - \bar{\lambda})^2 + (\lambda_3 - \bar{\lambda})^2}{\bar{\lambda}}}.$$

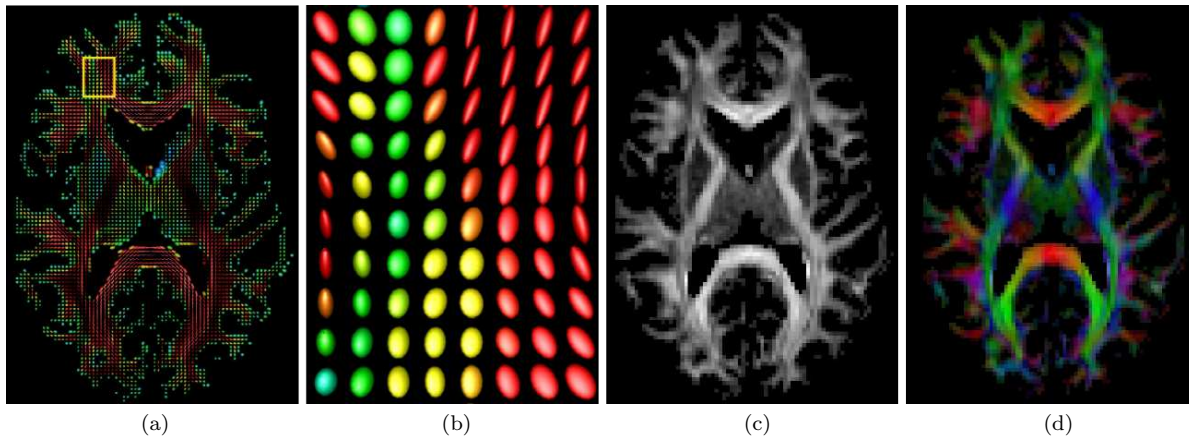


**Fig. 1.7** Diffusion Tensor Imaging (DTI). (a) DTI ellipsoids from an axial slice of the brain. (b) Zoom of highlighted box in (a). (c) Fractional Anisotropy (FA). (d) Colour FA where the colour components RGB represent the unit major eigenvector of the diffusion tensor  $\mathbf{e}_1 = [r, g, b]^T$  weighted by FA, or the colours indicate the preferential diffusion anisotropy directions.

- Westin et al. [73] proposed anisotropy measures to discern *linear*  $c_l$ , *planar*  $c_p$  and *spherical*  $c_s$  diffusion tensor shapes:

$$c_l = \frac{\lambda_1 - \lambda_2}{\sqrt{\lambda_1^2 + \lambda_2^2 + \lambda_3^2}}; \quad c_p = \frac{2(\lambda_2 - \lambda_3)}{\sqrt{\lambda_1^2 + \lambda_2^2 + \lambda_3^2}}; \quad c_s = \frac{3\lambda_3}{\sqrt{\lambda_1^2 + \lambda_2^2 + \lambda_3^2}}.$$

### 1.4.2 Beyond DTI

In DTI, the Gaussian assumption over-simplifies the diffusion of water molecules. While it is adequate for voxels in which there is only a single fiber orientation (or none), it breaks down for voxels in which there are more complex internal structures. This is an important limitation, since the resolution of dMRI acquisitions is between  $1\text{mm}^3$  and  $3\text{mm}^3$  while the physical diameter of fibers can be between  $1\mu\text{m}$  and  $30\mu\text{m}$  [54, 8]. Research groups currently agree that there is complex fiber architecture in most fiber regions of the brain [53]. In fact, it is currently thought that between one third to two thirds of imaging voxels in the human brain white matter contain multiple fiber bundle crossings [9]. This has led to the development of various High Angular Resolution Diffusion Imaging (HARDI) techniques [69] such as Q-Ball Imaging or Diffusion Spectrum Imaging for exploring the microstructure of biological tissues with greater accuracy.

HARDI samples q-space along as many directions as possible in order to reconstruct estimates of the true diffusion PDF – also referred as the EAP – of water molecules. This true diffusion PDF is model-free and can recover the diffusion of water molecules in any underlying fiber population. HARDI depends on the number of measurements  $N$  and the gradient strength ( $b$ -value), which directly affects acquisition time and signal to noise ratio in the signal.

#### 1.4.2.1 Diffusion Spectrum Imaging: Recovering the Diffusion EAP

*Diffusion spectrum imaging* (DSI) introduced by Wedeen et al. [71, 67] in 2000, was the first dMRI method that applied the q-space formalism to measure or estimate the EAP in biological tissue. The forte of the q-space formalism, where diffusion could reveal more than just the intrinsic properties like the diffusion coefficient, and show how it could probe the complex microstructure of the underlying tissue, became quickly apparent. Crossing fiber microstructures were clearly revealed by the geometric forms of the measured EAPs, or their characteristics. Such EAPs clearly represented non-free diffusion and were non-Gaussian. DSI was based on the Fourier Transform relationship between the signal and the EAP described in Eq. (1.17). Although in practice it couldn't satisfy the NGP condition required by the q-space formalism, DSI essentially imaged the q-space densely and reconstructed the EAP via a fast Fourier Transform (FFT). In fact,  $\delta \approx \Delta$  in the DSI experiments conducted in [71, 67, 72]. Nonetheless,

553 the angular results produced by such DSI experiments clearly spoke in favour of q-space imaging – as  
 551 seen in [58].

552 DSI, however, considered the modulus Fourier Transform:

$$P(\mathbf{r}) = \int |E(\mathbf{q})| \exp(-i2\pi\mathbf{q} \cdot \mathbf{r}) d\mathbf{q},$$

553 in place of the true Fourier Transform, justifying that in the case of pure diffusion the modulus Fourier  
 554 Transform is equal to the true Fourier Transform. This was done to counter biological motion such as  
 555 cardiac pulsation, which tended to contaminate the phase of the signal.

556 Initially visualizing iso-surfaces of the estimated EAP [71], DSI techniques later introduced the *orien-*  
 557 *tation distribution function* (ODF), to emphasize the angular results, which indicated underlying fibers.  
 558 Two ODFs were used, namely [72] (Fig. 1.8):

$$\Psi_{SA}(\mathbf{u}) = \int_{\mathbf{R}^+} P(r\mathbf{u})r^2 dr, \quad \mathbf{u} = \mathbf{r}/|\mathbf{r}|, \quad (1.23)$$

559 and the one introduced by Tuch [67]:

$$\Psi_T(\mathbf{u}) = \int_{\mathbf{R}^+} P(r\mathbf{u})dr, \quad \mathbf{u} = \mathbf{r}/|\mathbf{r}|. \quad (1.24)$$

560 However, DSI had severe acquisition setbacks. To correctly estimate the EAP, the q-space had to be  
 561 densely sampled, and also at very high b-values. The DSI sampling scheme was a Cartesian grid inside a  
 562 sphere in q-space, where both the radius of the sphere – the maximum b-value, and the number of grid-  
 563 points – the number of acquisitions played important roles in determining the accuracy of the estimated  
 564 EAP. For example in [71, 72], the maximum b-value was in the range of 20,000 s/mm<sup>2</sup>, and the number  
 565 of acquisitions were more than 500. In comparison, DTI acquisitions are done for b-values of 1000 s/mm<sup>2</sup>,  
 566 and only require a minimum of 6 acquisitions. These demanding requirements played unfavourably for  
 567 DSI, since its clinical viability was near impossible.

568 However, DSI was the proof of concept for q-space imaging, which quickly became the popular approach  
 569 for dMRI, and gave rise to a plethora of techniques for estimating complex EAPs or their characteristics  
 570 like the ODF. These q-space techniques were developed to overcome the acquisition limitations of DSI.

#### 571 1.4.2.2 Q-Ball Imaging: Emphasizing the Anisotropic Diffusion Orientation Information

572 *Q-Ball Imaging* (QBI) was proposed by Tuch [67, 68] spurred by the facts that DSI had severe acquisition  
 573 requirements, and that the DSI result of interest wasn't the estimated EAP itself, but rather its radial  
 574 projection – the ODF, which emphasized angular details. His idea was to retrieve the same angular result  
 575 with reduced acquisition requirements. His initial attempt was the model based multi-tensor approach  
 576 which was stricken with instabilities induced by the assumed model. Therefore, he proposed QBI, a

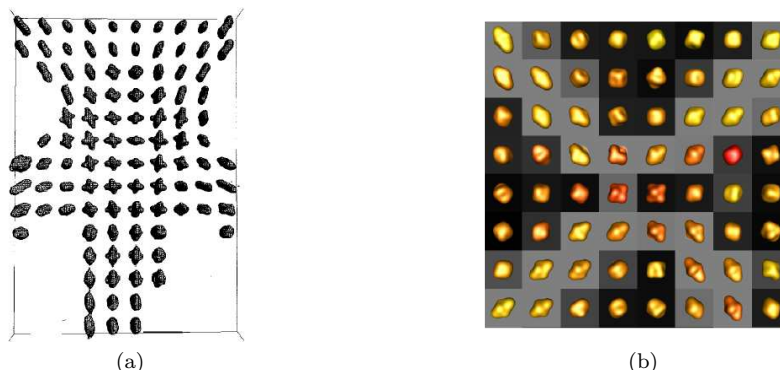


**Fig. 1.8** Diffusion Spectrum Imaging & Q-Ball Imaging. (a) DSI diffusion PDFs from [71]. Corticospinal tract (orientations sup.-inf.) and pontine decussation (left-right). (b) ODFs, estimated from an analytical q-ball approach, such that they represent the angular marginal distributions of the true and unknown EAPs (biological rat phantom).

577 model free method that sampled q-space only on a sphere or q-shell with fixed q-radius with high angular  
578 resolution.

579 QBI like DSI is based on the q-space formalism and shows promising results, although like DSI, in  
580 practice it cannot satisfy the NGP condition [67]. However, QBI became a forerunner to a plethora of  
581 q-space methods that attempted to reconstruct the EAP or its characteristics from partial sampling of  
582 the q-space. QBI, itself maps spherical acquisitions in q-space to the ODF – a spherical function in real  
583 space.

584 QBI is based on the *Funk Radon transform* (FRT), which is a mapping from a sphere to a sphere  
585  $\mathcal{G} : S^2 \rightarrow S^2$ . To a point on the sphere, called the pole, the FRT of a spherical function  $f$ , assigns the  
586 value of the integral of the spherical function along the equator on the plane that has for normal the  
587 vector connecting the centre of the sphere to the pole:

$$\mathcal{G}[f(\mathbf{u})](\mathbf{u}) = \int_{S^2} f(\mathbf{u}) \delta(\mathbf{u}^T \mathbf{w}) d\mathbf{w},$$

588 where  $\mathbf{u}, \mathbf{w} \in S^2$ . Using the Fourier slice theorem, Tuch was able to show that the FRT of the signal  
589 acquired on a q-sphere was equal to the ODF in Eq. (1.24) blurred by a zeroth-order Bessel function,  
590 where the blurring or the width of the Bessel function was inversely proportional to the radius of the  
591 acquisition q-sphere.

592 QBI, therefore, made it possible to reconstruct the angular result of DSI, i.e. the ODF, with fewer  
593 acquisitions and without assuming any models. QBI was further boosted by [2, 32, 24], where an analytical  
594 solution was proposed, by using the *spherical harmonic* (SH) basis. It was shown that the SHs are the  
595 eigenfunctions of the FRT [24]. Letting  $Y_l^m$  denote the SH of order  $l$  and degree  $m$  ( $m = -l, \dots, l$ ), a  
596 modified real and symmetric SH basis is defined. For even order  $l$ , a single index  $j$  in terms of  $l$  and  $m$   
597 is used such that  $j(l, m) = (l^2 + l + 2)/2 + m$ . The modified basis is given by:

$$Y_j = \begin{cases} \sqrt{2} \cdot \text{Re}(Y_l^{|m|}), & \text{if } m < 0 \\ Y_l^m, & \text{if } m = 0, \\ \sqrt{2} \cdot (-1)^{m+1} \cdot \text{Im}(Y_l^m), & \text{if } m > 0 \end{cases} \quad (1.25)$$

598 where  $\text{Re}(Y_l^m)$  and  $\text{Im}(Y_l^m)$  represent the real and imaginary parts of  $Y_l^m$  respectively. This modified  
599 basis is designed to be real, symmetric and orthonormal, and it is then possible to obtain an analytical  
600 estimate of the ODF in Eq. (1.24) with [24]:

$$\Psi_T(\mathbf{u}) = \sum_{j=1}^L \underbrace{2\pi P_{l(j)}(0) c_j}_{c'_j} Y_j(\mathbf{u}), \quad (1.26)$$

601 where  $L = (l+1)(l+2)/2$  is the number of elements in the modified SH basis,  $c_j$  are the SH coefficients  
602 describing the input HARDI signal,  $P_{l(j)}$  is the Legendre polynomial of order  $l$  that is associated with  
603  $j$ th element of the modified SH basis and  $c'_j$  are the SH coefficients describing the ODF  $\Psi_T$ .

604 Aganj et al. [1] recently proposed an analytical solution to QBI using SHs to compute the ODF in Eq.  
605 (1.23), under a mono-exponential assumption of the signal. The ODF in Eq. (1.23) takes into account  
606 the solid angle factor during the radial integration, therefore, it is a true marginal density function of the  
607 EAP. This solution was also proposed by Vega et al. in [66]. The ODF in Eq. (1.24) proposed by Tuch  
608 on the other hand doesn't account for this solid angle, and therefore needs to be numerically normalized  
609 after estimation [68] (Fig. 1.8).

## 610 1.5 Computational Framework for Processing Diffusion MR Images

611 Diffusion MRI is a rich source of complex data in the form of images. Processing dMRI data poses a  
612 challenging problem since diffusion images can range from scalar images such as DWIs, where each voxel  
613 contains a scalar grey-level value, to tensor images such as in DTI, where each voxel contains a 2nd order  
614 tensor, to more complex and generic function images such as in DSI or QBI, where each voxel contains a  
615 diffusion function such as the EAP in DSI or a spherical function such as the ODF in QBI, represented

616 as coefficients in a particular basis of choice – such as the SH basis. Therefore, processing such higher  
 617 dimensional images requires sophisticated mathematical and computational tools.

618 Processing diffusion images also forms an important part of the dMRI pipeline from acquisition to ex-  
 619 traction of meaningful physical and medical information from the data. Operations such as regularization  
 620 are important for denoising diffusion images as they render the tensor field in DTI or ODF field in QBI  
 621 more coherent and therefore greatly improve the results of post-processing algorithms such as tractog-  
 622 raphy. A rich body of literature for regularizing tensor fields in DTI can be found in [51, 3, 15, 50, 46].  
 623 The capacity to segment tensor images or ODF images makes it possible to identify and reconstruct  
 624 white matter structures in the brain such as the corpus callosum, which is not possible from simple scalar  
 625 MR images. However, the extension of such operations from scalar images to tensor fields or ODF fields  
 626 requires the correct mathematical definitions for spaces of tensors (or EAPs or ODFs) with the appropri-  
 627 ate metric. In this section we will present the tools required to process tensor images (DTI), which has  
 628 seen extensive mathematical development recently. In particular we will present appropriate metrics for  
 629 the space of symmetric positive definite matrices (or diffusion tensors)  $\mathcal{Sym}_n^+$ , an estimation algorithm  
 630 for DTI that ensures that the DT is estimated in  $\mathcal{Sym}_n^+$  using the Riemannian metric of  $\mathcal{Sym}_n^+$  and a  
 631 segmentation algorithm that uses the Riemannian metric of  $\mathcal{Sym}_n^+$  to segment regions in a tensor field.

### 632 *1.5.1 The Affine Invariant Riemannian Metric for Diffusion Tensors*

633 Diffusion tensors are  $3 \times 3$  symmetric matrices. However, since negative diffusion is non-physical these  
 634 matrices are also required to be positive definite. In other words DTs belong to the space  $\mathcal{Sym}_3^+$  of  $3 \times 3$   
 635 symmetric positive definite matrices, which is a non-Euclidean space. Therefore an appropriate metric  
 636 needs to be defined on this space which would render it into a Riemannian manifold and which would  
 637 permit to constrain all operations naturally to  $\mathcal{Sym}_3^+$  by using Riemannian geometry.  $\mathcal{Sym}_3^+$  naturally  
 638 inherits the Euclidean and the Frobenius metrics from the space of all matrices, however,  $\mathcal{Sym}_3^+$  is neither  
 639 complete nor closed under these metrics.

640 A number of works have recently proposed the affine invariant Riemannian metric for  $\mathcal{Sym}_n^+$  which  
 641 has been used extensively to compute on DTs [45, 51, 40]. In [51] the Riemannian metric is derived to be  
 642  $g_{ij} = g(X, Y) = \langle X, Y \rangle_{\mathbf{S}} = \text{tr} \left( \mathbf{S}^{-\frac{1}{2}} X \mathbf{S}^{-\frac{1}{2}} Y \mathbf{S}^{-\frac{1}{2}} \right)$ ,  $\forall \mathbf{S} \in \mathcal{Sym}_3^+$  and with  $X, Y \in T_{\mathbf{S}} \mathcal{Sym}_3^+ = \mathcal{Sym}_3$  the  
 643 tangent space at  $\mathbf{S}$ . The geodesic distance between DTs induced by this metric can be computed to be:

$$644 \mathcal{D}_{Rm}(\mathbf{S}_1, \mathbf{S}_2) = \sqrt{\frac{1}{2} \text{tr} \left( \ln^2 \left( \mathbf{S}_1^{-1/2} \mathbf{S}_2 \mathbf{S}_1^{-1/2} \right) \right)}. \quad (1.27)$$

645 An equally well known metric for  $\mathcal{Sym}_n^+$  is the Log-Euclidean metric [3]. Although it isn't affine invariant  
 646 and only similarity invariant, computationally it is more efficient than the affine invariant Riemannian  
 metric and resembles closely the latter. The distance between DTs induced by this metric is:

$$647 \mathcal{D}_{LE}(\mathbf{S}_1, \mathbf{S}_2) = \sqrt{\frac{1}{2} \text{tr} \left( (\ln(\mathbf{S}_1) - \ln(\mathbf{S}_2))^2 \right)}. \quad (1.28)$$

### 647 *1.5.2 Estimation of DTs in $\mathcal{Sym}_3^+$ Using the Riemannian Metric*

648 Using the appropriate Riemannian metric and geometry for  $\mathcal{Sym}_3^+$  can constrain all operations to  $\mathcal{Sym}_3^+$ .  
 649 For example using the Riemannian metric for DTI estimation can ensure that the DTs are positive definite  
 650 or that no negative diffusion will be estimated even in the presence of noisy DWIs. This can be done by  
 651 using the logarithmically transformed version of the Stejskal-Tanner equation (Eq. 1.13) and considering  
 652 its explicit least square minimization  $E(\mathbf{D}) = \frac{1}{2} \sum_{i=1}^N \left( \frac{1}{b} \ln \left( \frac{S_i}{S_0} \right) + \mathbf{g}_i^T \mathbf{D} \mathbf{g}_i \right)^2$ . The gradient of this least  
 653 square functional using the affine invariant Riemannian metric can be shown to be [40]:

$$\nabla E(\mathbf{D}) = \sum_{i=1}^N \left( \frac{1}{b} \ln \left( \frac{S_i}{S_0} \right) + \mathbf{g}_i^T \mathbf{D} \mathbf{g}_i \right) \cdot (\mathbf{D} \mathbf{g}_i) (\mathbf{D} \mathbf{g}_i)^T. \quad (1.29)$$

654 Furthermore the Euclidean gradient descent algorithm required for optimization has to be appropriately  
 655 replaced by a Riemannian geodesic descent algorithm to respect the Riemannian geometry of  $Sym_3^+$ .

### 656 1.5.3 Segmentation of a Tensor Field

657 The goal of segmenting a tensor field or an image of DTs is to compute the optimal 3D surface separating  
 658 an anatomical structure of interest from the rest of the tensor image (see Fig. 1.9). To do this we follow  
 659 the method proposed in [23]. The idea will be to treat the tensor field as a field of Gaussian probability  
 660 density functions and to utilize the affine invariant Riemannian metric on  $Sym_3^+$ , which also forms a  
 661 Riemannian metric in the space of Gaussian density functions, to compute the segmentation boundary.  
 662 Therefore, a DT at the point  $x$  in the image corresponds to the 3D Gaussian distribution  $N(x, r)$ .

663 Using the level-set approach and the optimal boundary  $\Gamma$  between the object of interest  $\Omega_1$  and the  
 664 background  $\Omega_2$ , the level-set  $\phi : \Omega_1 \cup \Omega_2 \rightarrow \mathbb{R}$  can be defined as:

$$\begin{cases} \phi(x) = 0, & \text{if } x \in \Gamma \\ \phi(x) = \mathcal{D}_E(x, \Gamma), & \text{if } x \in \Omega_1 \\ \phi(x) = -\mathcal{D}_E(x, \Gamma), & \text{if } x \in \Omega_2 \end{cases} \quad (1.30)$$

665 where  $\mathcal{D}_E(x, \Gamma)$  represents the Euclidean distance between  $x$  and  $\Gamma$ . Then according to the geodesic  
 666 active regions model along with a regularity constraint on the interface, the optimal boundary  $\Gamma$  or the  
 667 segmentation of the tensor field is obtained by minimizing the functional:

$$E(\phi, P_1, P_2) = \nu \int_{\Omega = \Omega_1 \cup \Omega_2} |\nabla H_\varepsilon(\phi)| dx - \int_{\Omega} H_\varepsilon(\phi) \ln(P_1(N(x, r))) dx - \int_{\Omega} (1 - H_\varepsilon(\phi)) \ln(P_2(N(x, r))) dx, \quad (1.31)$$

668 where  $H_\varepsilon(\cdot)$  is a regularized version of the Heaviside function [23], and  $P_1$  and  $P_2$  are the probability  
 669 distributions of the set of Gaussian distributions  $N(x, r)$  in  $\Omega_1$  and  $\Omega_2$  respectively.

670 Equation (1.31) can be solved computationally by assuming the distributions  $P_1$  and  $P_2$  themselves to  
 671 be Gaussians distributions. However, that would require the computation of the mean and the standard  
 672 deviation of the set of 3D Gaussian distributions  $N(x, r)$  constituting  $\Omega_1$  and  $\Omega_2$ . This mean and standard  
 673 deviation of a set of Gaussian distributions would require a metric to be defined on the space of Gaussian  
 674 distributions. A number of examples are provided in [23] – the Euclidean metric, the Kullback-Leibler  
 675 divergence, and the Riemannian metric. We reproduce here only the final example.

676 Using the affine invariant Riemannian metric on  $Sym_3^+$ , which also forms a Riemannian metric on  
 677 the space of 3D Gaussian distributions  $N(x, r)$ , it is possible to compute the mean distribution  $\bar{N}(X, r)$   
 678 of a set of Gaussian distributions by a process of Riemannian geodesic descent – a modified gradi-

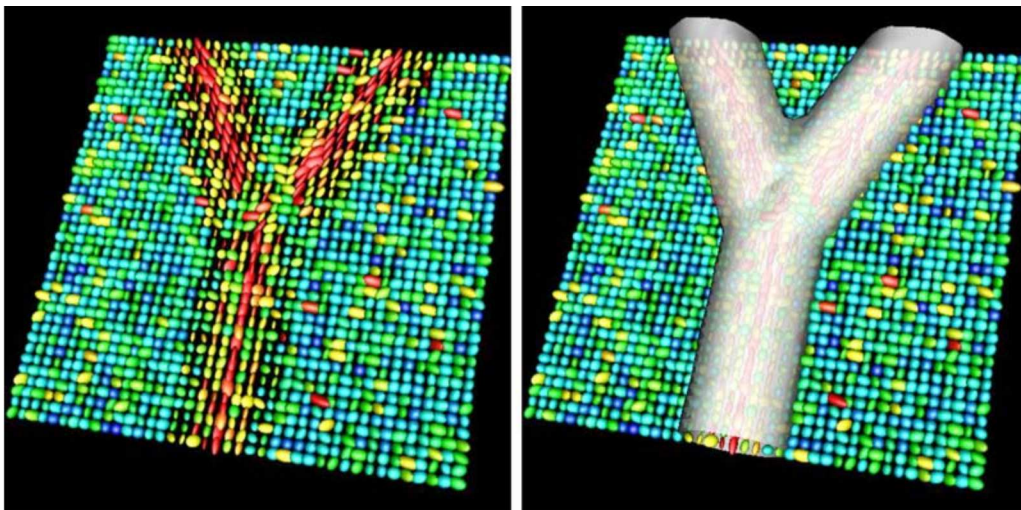


Fig. 1.9 Tensor field segmentation on a synthetic dataset simulating DTI [41].

ent descent process. Similarly the empirical covariance matrix relative to the mean  $\bar{N}$  is defined to be  $\Lambda_{Rm} = \frac{1}{n-1} \sum_{i=1}^n \beta_i \beta_i^T$ , with  $\beta_i = \bar{N} \ln(N_i^{-1} \bar{N})$  which is the gradient of the squared geodesic distance  $\nabla \mathcal{D}_{Rm}^2(N_i, \bar{N})$  in vector form. Using these it is possible to define a generalized Gaussian distribution over the space of 3D Gaussian distributions with a covariance matrix  $\Lambda_{Rm}$  of small variance  $\sigma^2 = \text{tr}(\Lambda_{Rm})$ :

$$P_{Rm}(N | \bar{N}, \Lambda_{Rm}) = \frac{1 + O(\sigma^3) + \varepsilon(\sigma/\eta)}{\sqrt{(2\pi)^{m(m+1)/2} |\Lambda_{Rm}|}} \exp\left(\frac{-\beta^T \gamma \beta}{2}\right) \quad \forall N \in \text{Sym}_3^+, \quad (1.32)$$

where  $\gamma = \Lambda_{Rm}^{-1} - \mathcal{R}/3 + O(\sigma) + \varepsilon(\sigma/\eta)$  with  $\mathcal{R}$  as the Ricci curvature tensor at  $\bar{N}$ ,  $\eta$  as the injection radius at  $\bar{N}$  and  $\varepsilon$  such that  $\lim_{0^+} x^{-\beta} \varepsilon(x) = 0 \forall \beta \in \mathbb{R}^+$ .

## 1.6 Tractography: Inferring the Connectivity

When DTI/DSI/QBI is performed on the brain, the DT/EAP/ODF – hereafter referred to as the *spherical diffusion function* (SDF), is a local indicator of coherent structures or fiber bundles in the cerebral white matter. However, the process of reconstructing the global structures of fiber bundles by connecting the local information is known as fiber tracing or *tractography*. Tractography graphically reconstructs the connectivity of the cerebral white matter by integrating along the direction indicated by the local geometry of the SDF. It is a modern tool that is unique in the sense that it permits an indirect dissected visualization of the brain in vivo and non-invasively [16]. The underpinnings of tractography are also based on the fundamental assumption of dMRI – the diffusion of water molecules is hindered to a greater extent perpendicular to coherent fiber bundle structures than parallel to these. Therefore, following the geometry of the local diffusion function and integrating along reveals the continuous dominant structure of the fiber bundle. However, in spite of the gain due to its non-invasive nature, tractography can only infer such structures indirectly. Therefore, tractography is acutely sensitive to the local geometry and the error is cumulative. The correct estimation of the local geometry is crucial.

Deterministic tractography is a well established tool that has seen considerable success in researching neurological disorders [20]. Deterministic tractography begins from a seed point and traces along the dominant fiber direction by locally connecting the “fiber” vectors or mathematically becoming tangent to these. Classically the major eigenvector of the diffusion tensor in DTI represented these “fiber” vectors [47, 7, 38]. However, since DTI is ambiguous and cannot accurately describe the fiber directions in regions with complex fiber configurations, DTI tractography, in spite of its successful usage, is known to be prone to errors. Hence the trend in recent years to extend tractography to complex shaped SDFs that describe the underlying fiber directions more accurately [67, 72, 25].

Probabilistic tractography was proposed to address the reliability of deterministic tractography which remains sensitive to a number of parameters. The concept and output of probabilistic tractography is, however, subtly different from deterministic tractography. While the latter attempts to find the connectivity between two regions, the former measures the likelihood that two regions are connected, or it provides a connectivity confidence. Given the capabilities and ambiguities of dMRI acquisition and reconstruction schemes of today, due to partial voluming, noise, etc., probabilistic tractography provides a more complete statement. However, probabilistic tractography is also computationally more expensive than deterministic tractography.

### 1.6.1 Deterministic Tractography

Of the many deterministic tractography algorithms, the continuous *streamline tractography* is a widely used scheme. The continuous version of streamline tractography [7] defined for DTI, considers a fiber tract as a 3D space curve parametrized by its arc-length,  $\mathbf{r}(s)$ , and describes it by its Frenet equation:

$$\frac{d\mathbf{r}(s)}{ds} = \mathbf{t}(s) = \varepsilon_1(\mathbf{r}(s)), \quad (1.33)$$

where  $\mathbf{t}(s)$  the tangent vector to  $\mathbf{r}(s)$  at  $s$  is equal to the unit major eigenvector  $\varepsilon_1(\mathbf{r}(s))$  of the diffusion tensor at  $\mathbf{r}(s)$ . This implies that fiber tracts are locally tangent to the dominant eigenvector of the



721 diffusion tensor at every spatial position. The differential equation Eq. (1.33) along with the initial  
 722 condition  $\mathbf{r}(0) = \mathbf{r}_0$  means that starting from  $\mathbf{r}_0$ , a fiber can be traced by continuously integrating Eq.  
 723 (1.33) along the direction indicated locally by the major eigenvector of the diffusion tensor at that point.

724 However, integrating Eq. (1.33) requires two things – first, a spatially continuous tensor (or SDF) field,  
 725 and second, a numerical integration scheme. In [7], the authors proposed two approaches for estimating a  
 726 spatially continuous tensor field from a discrete DTI tensor field, namely approximation and interpolation.  
 727 They also proposed the Euler’s method, the 2nd order Runge-Kutta method, and the adaptive 4th order  
 728 Runge Kutta method as numerical integration schemes. Finally, for stopping they proposed four criteria  
 729 – the tracts are within the image volume, the tracts are in regions with FA value higher than a threshold,  
 730 the curvature of a tract is smaller than a threshold, and that a tract is better aligned with the major  
 731 eigenvector in the next spatial location than any of the two other eigenvectors.

732 The streamline tractography algorithm can be adapted to SDFs with multiple maxima (EAP/ODF  
 733 etc.) by modifying Eq. (1.33) to:

$$\frac{d\mathbf{r}(s)}{ds} = \eta_{\theta_{min}}(\mathbf{r}(s)), \quad \mathbf{r}(0) = \eta_{max}(0) \quad (1.34)$$

734 where  $\eta_i(\mathbf{r}(s))$  are all the unit maxima vectors of the SDF at  $\mathbf{r}(s)$ ,  $\eta_{max}$  is the unit maximum vector whose  
 735 function value is the largest amongst all the  $\eta_i$ , and  $\eta_{\theta_{min}}$  is the unit maximum vector in the current  
 736 step that is most collinear to the unit maximum vector followed by the integration in the previous step.  
 737 Equation (1.34) and the initial condition state that at the starting point the integrating begins along the  
 738 dominant maximum direction, and at each consecutive step first all the maxima of the SDF are detected  
 739 and the maximum direction most collinear to the maximum direction from the previous integration step  
 740 is chosen to move forward in the integration.

741 The maximum direction most collinear to the previously chosen maximum direction can be chosen by  
 742 computing the dot product between the previously chosen maximum direction and all the maxima of the  
 743 current step, and by considering the absolute values of the dot products. Hence, the maximum chosen for  
 744 the next integration direction is the maximum whose absolute value of its dot product with the previously  
 745 chosen maximum direction is the largest. Also to avoid erratic forward and backward steps during the  
 746 integration, if the value of the dot product is negative, it is necessary to flip the unit maximum direction  
 747 to point it consistently along the fiber direction, just like in [7].

748 Since streamline tractography requires a continuous field of SDFs for integrating Eq. (1.34), a contin-  
 749 uous field of SDFs can be computed from a simple Euclidean interpolation of the SDFs when the SDFs  
 750 are expressed in the SH basis. The Euclidean interpolation in the SH basis is equivalent to the L2-norm  
 751 interpolation of the SDFs, since the SHs form an orthonormal basis [26].

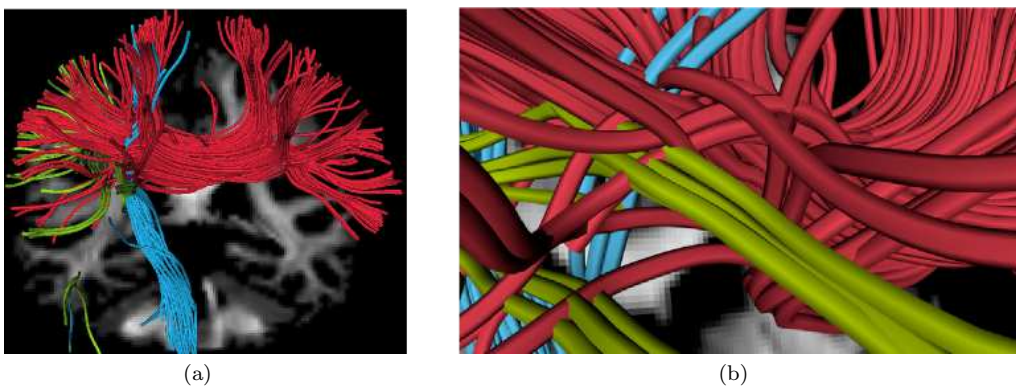


**Fig. 1.10** Deterministic Tractography on ODFs. (a) Three fiber bundles are traced, starting from different seed regions. Red: seeds in the CC (left-right). Blue: seeds in the CST (superio-inferior). Green: seeds in the SLF (anterio-posterior). (b) Zoom into crossing region.

## 1.6.2 Probabilistic Tractography

General SDF-based (ODF etc.) probabilistic tractography have recently been published in the literature [52, 48, 9, 33, 57, 35, 60, 17] to generalize several existing DT-based methods. First, in [35] parametric spherical deconvolution is used as the SDF [65] and in [9] a mixture of Gaussian model is used to extend the probabilistic Bayesian DT-based tracking [10]. Related to these techniques, [33] uses a Bayesian framework to do global tractography instead of tracking through local orientations. In [52], Monte Carlo particles move inside the continuous field of q-ball diffusion ODF and are subject to a trajectory regularization scheme. In [48], an extension to their DT-based approach [49] is also proposed using a Monte Carlo estimation of the white matter geometry and recently, a Bingham distribution is used to model the peak anisotropy in the fiber distributions [60]. Finally, in [17], large number of M-FACT QBI streamlines are reconstructed and all pathways are reversed-traced from their end points to generate of map of connection probability. In this chapter, a new probabilistic algorithm is presented based on the ODF using a Monte Carlo random walk algorithm.

The new algorithm is an extension of the random walk method proposed in [36] to use the distribution profile of the fiber ODF. It starts off a large number of particles from the same seed point and lets the particles move randomly according to the local ODF estimate,  $F$ , and counts the number of times a voxel is reached by the path of a particle. This yields higher transitional probabilities along the main fiber directions. The random walk is stopped when the particle leaves the white matter mask.

For each elementary transition of the particle, the probability for a movement from the seed point  $x$  to the target point  $y$  in direction  $\mathbf{u}_{xy}$  is computed as the product of the local ODFs in direction  $\mathbf{u}_{xy}$ , i.e.

$$P(x \rightarrow y) = F(\mathbf{u}_{xy})_x \cdot F(\mathbf{u}_{xy})_y \quad (1.35)$$

where  $P(x \rightarrow y)$  is the probability for a transition from point  $x$  to point  $y$ ,  $F(\mathbf{u}_{xy})_x$  is the ODF at point  $x$  in direction  $xy$  (by symmetry, direction  $xy$  and  $yx$  are the same).

The transition directions in the local model are limited to 120 discrete directions corresponding to the angular sampling resolution of the acquired brain data and the step size of the particle step was fixed to 0.5 times the voxel size. A trilinear interpolation of the ODF was used for the subvoxel position and a white matter mask computed from a minimum FA value of 0.1 and a maximum ADC value of 0.0015 was used. A total of 100000 particles were tested for each seed voxel. The connectivity of any given voxel with the seed voxel is estimated by the number of particles that reach the respective voxel, called a *tractogram*.

## 1.7 Clinical Applications

Diffusion MRI has now proved to be extremely useful for studying the normal and pathological human brain [11, 27] and for improving diagnosis and therapy of brain diseases. It has led to many applications in clinical diagnosis of neurological diseases and disorders, neuroscience applications in assessing connectivity of different brain regions and more recently, therapeutic applications, primarily in neurosurgical planning. Indeed, the sensitivity of diffusion measures to changes in the white matter have led to a wealth of clinical studies using second order diffusion tensor imaging as an in vivo clinical marker and dMRI has opened up a landscape of discoveries for neuroscience and medicine through research and clinical exploration of fiber connectivity and CNS diseases.

The dMRI models and tools presented in this chapter are at the heart of what is strongly needed to better recover, study and understand the anatomical connectivity of the normal and pathological human CNS. These dMRI methodological developments have already been applied in many places to better describe, characterize and quantify abnormalities within the CNS white matter and develop in vivo markers for diseases in clinical neuroscience.

The first and most successful application of dMRI since the early 1990s has been in acute brain ischemia, that emerged from the discovery of Moseley et al. that water diffusion immediately drops after the onset of an ischemic event, when brain cells undergo swelling through cytotoxic edema. This result was later confirmed by different groups using animal models and human patients with stroke.

Since then, many important CNS diseases have attracted the interest of dMRI researchers. Hence, DTI has appeared as a promising tool to look at brain maturation and development, especially to monitor the myelination process, as well as changes in connectivity in relation to functional disorders. Indeed, it

802 has been shown by many studies that the degree of diffusion anisotropy in white matter increases during  
803 the myelination process, so that dMRI could be used to assess brain maturation in children, newborns  
804 or premature babies, as well as to characterize white matter disorders in children. DTI has now been  
805 used for more than ten years to look, in vivo, at the disorganization of white matter in schizophrenia,  
806 which is thought to come from myelin abnormalities. Most neuroimaging studies of schizophrenia have  
807 used second order DTI so far, as a means to quantify the integrity of the white matter.

808 Alzheimer's and Parkinson's diseases, two of the most important neurodegenerative diseases, as well  
809 as others like multiple sclerosis have characteristic abnormalities in the microstructure of brain tissues  
810 that are not apparent and cannot be revealed reliably by standard imaging techniques. Diffusion MRI  
811 can reveal these co-lateral damages to the fibers of the CNS white matter that connect different brain  
812 regions.

813 We in the Athena Project Team, INRIA, France, are currently focusing on the use of ultra high field  
814 MRI (3T and 7T) techniques for investigating the structural disorders of the brain stem and of the  
815 central deep nuclei in the field of Parkinson's syndrome. This work aims to identify the biomarkers of the  
816 pathology by benefitting from the latest developments in the domain of ultra high fields and from the latest  
817 image processing innovations in the field of diffusion imaging based on high angular resolution models.  
818 Determining the biomarkers for the various forms of Parkinson's disease using high field systems will surely  
819 open the way for developing new diagnosis tools at lower field strengths and thus make them available to  
820 a clinical environment. Deep brain nuclei are important structures that are involved in a large array of  
821 behaviors, such as locomotion, eye-movement, or sleep. Damage to these structures leads to movement  
822 disorders such as Parkinson's disease. To date, except for the larger striato-pallidal complex, there are  
823 no reliable imaging markers of small deep nuclei. With dMRI and refinements of neuroimaging methods  
824 and higher field magnets, imaging of these nuclei has become possible. Together with our collaborators at  
825 the Center of Neuroimaging Research (CENIR, Paris, France) and CEA Neurospin (Saclay, France), we  
826 are currently conducting a series of experiments in normal volunteers and in patients with basal ganglia  
827 pathology to characterize deep brain structures and study the structural disorders of the brainstem in  
828 the case of Parkinsonian syndromes. More precisely, we are involved in the data analysis part with the  
829 objective to detect the anatomical connectivity of the brainstem structures and their connectivity to  
830 the brain and we hope to find new neuroimaging markers of deep brain nuclei that could be used for  
831 the diagnosis of Parkinsonian syndromes at an early stage. Possible extension and improvements of the  
832 tractography algorithms presented here would be necessary to obtain a satisfactory spatial resolution for  
833 identifying the anatomical network involved in Parkinson's disease and improve the characterization of  
834 lesions of deep brain structures.

835 An important application where dMRI is expected to significantly impact in the close future is Trau-  
836 matic Brain Injury (TBI), which is the damage caused to the brain due to external mechanical force, such  
837 as rapid acceleration or deceleration, falls, motor vehicle accidents, impact or penetration by a projectile.  
838 The worst injuries can lead to permanent brain damage or death. Because a sudden and violent trauma  
839 to the head can cause injury to and shearing of the white matter fibers, it's indeed possible to use dMRI  
840 to examine the integrity of white matter that is especially vulnerable to TBI. This opens the way to  
841 exciting and challenging problems to quantify and qualify structural changes in white matter.

842 To this date, a large number of dMRI clinical studies of TBI only uses simple scalar diffusion mea-  
843 surements such as FA and/or MD to characterize the structural abnormalities present along a given fiber  
844 pathway to identify pathologies and compare patients with healthy controls. This clearly opens the road  
845 to many exciting and challenging problems to examine with more elaborate diffusion models the white  
846 matter's integrity and to better quantify and qualify structural changes in white matter.

847 Through our collaborations with clinical partners and our development of innovative tensor and HARDI  
848 processing methods, we are convinced that we can advance further our ability to better understand the  
849 architecture of the CNS and help to prove that dMRI can provide a relevant source of useful information,  
850 such as in vivo markers of diseases in clinical neuroscience.

851 Efficient and better tools are therefore more than welcome for undertaking a more systematic study of  
852 these abnormalities. For instance, HARDI's improved signal-to-noise ratio can image fiber paths with  
853 extraordinary angular detail, identifying more relevant anatomical features, connections and disease  
854 biomarkers not seen with conventional MRI.

855 Moving from quantitative comparisons of scalar values derived from second order diffusion tensors in  
856 voxels or along existing pathways, to more relevant measures based on higher order diffusion models and  
857 demonstration of qualitative changes in white matter anatomy is extremely challenging.

Therefore, key challenges to tackle include defining new biomarkers related to the quantities, scalar or not, that could be retrieved from High Order Tensors, HARDI, Q-Ball or the EAP to better describe and characterize the biological tissue being analyzed.

Overall, one of the main objectives now is to apply the new methodological developments to improve dMRI as a clinical tool and make it more apt in characterizing and quantifying abnormalities within CNS white matter and to develop better neuroimaging markers for the diagnosis of CNS neurodegenerative diseases. There is a consensus in the neuroimaging field that more elaborate models and HARDI measures will certainly advance research in a large number of CNS diseases.

We are confident that the recent development of novel mathematical analysis tools for dMRI and HARDI will certainly result in fundamental advances for research on stroke, multiple sclerosis, amyotrophic lateral sclerosis, Alzheimer's and Parkinson's diseases, HIV/AIDS, neurosurgery, tumor growth modeling or neuropsychiatric disorders like schizophrenia. Moreover, our understanding of the development of the human brain, the effect of aging or the organization of anatomo-functional networks has already started to greatly benefit from the unprecedented insight that dMRI provides into the brain's microstructure.

## 1.8 Conclusion

In this chapter we presented an overview of the mathematical tool and framework of dMRI. Diffusion MRI is unique in its capacity at inferring the microstructure of the cerebral white matter in vivo and non-invasively, albeit in an indirect fashion. We first presented a quick perusal of the brain its general structure and organization, the tissues constituting it, and in highlight, its major neuronal pathways interconnecting its various regions. These are central for understanding the diffusion of water molecules in the brain, and for understanding the usefulness of dMRI in studying the brain. The Brownian motion of the water molecules contained in the brain is hindered in the white matter by its fibrous structures in a particular fashion. While the diffusion of water molecules is greatly hindered perpendicular to these structures, the diffusion parallel to these structures is relatively less affected. In other words the diffusing water molecules probe the white matters microstructure. Therefore, since dMRI is sensitive to the diffusion of water molecules, it is used to measure the constrained or anisotropic diffusion of water molecules in the white matter, to infer its major axon fiber bundles non-invasively.

Next we presented the fundamentals of the NMR phenomenon, the diffusion NMR experiment, and reviewed three important diffusion MRI reconstruction algorithms. The NMR experiment can recover several different physical properties from samples which contain spin bearing particles by simply applying a set of magnetic fields and gradients. This forms the core of the non-invasive nature of MRI. However, NMR can only examine a tiny region of a sample or a single spin ensemble and cannot image an entire biological specimen. This is made possible by the spatial encoding technique of MRI, which allows to spatially encode various juxtaposed regions or spin ensembles where NMR can be applied independently. This is done in MRI again using magnetic gradients. Therefore, this allows MRI to examine entire biological specimen, like the brain or the body, in vivo and non-invasively.

One of the properties that NMR can be sensitized to is the Brownian motion of the spin bearing particles in a sample. Therefore, NMR can be used to measure the diffusion properties of a sample by modelling the diffusion of the spin bearing particles in the sample. Since diffusion has been historically modelled in two different ways, namely the Ficks phenomenological laws of diffusion and Einsteins random walk model of Brownian motion, the diffusion NMR signal is also modelled in two ways, namely the Stejskal-Tanner formulation and the q-space formalism.

DTI was the first dMRI technique that was proposed to infer the tissue microstructure. It is the most commonly used technique since its mathematical framework is simple, it has few acquisition requirements and has a number of powerful and practical applications. However, it is limited in regions with microstructural heterogeneity. Many higher order techniques have been therefore proposed recently in dMRI to overcome this limitation of DTI. Of these we presented DSI and QBI, and in particular the ODF.

Diffusion MRI data represents images that contain complex mathematical objects. Recently the computational framework of mathematical tools required to process such images has been vastly improved. We presented the appropriate metrics, in particular the Riemannian metric for  $Sym_n^+$ , an estimation algorithm and a segmentation framework using this metric for DTI.

911 DTI, ODFs and other general SDFs represent the local microstructure of the cerebral white matter  
 912 in each voxel. As the final mathematical tools we presented tractography algorithms which spatially  
 913 integrate anisotropy information to reconstruct more global structures such as white matter fiber tracts.  
 914 Tractography is a unique tool which permits one to indirectly dissect and visualize the brain's white  
 915 matter in vivo and non-invasively

916 Finally we concluded the chapter with an overview of major clinical applications to highlight and  
 917 emphasize the usefulness and strengths of dMRI.

## 918 1.9 Online Resources: Softwares and Databases

919 [medINRIA](http://www-sop.inria.fr/asclepios/software/MedINRIA/) <http://www-sop.inria.fr/asclepios/software/MedINRIA/>

920 medINRIA is a multi-platform medical image processing and visualization software, and it's free.  
 921 Through an intuitive user interface, medINRIA offers from standard to cutting-edge processing func-  
 922 tionalities for your medical images such as 2D/3D/4D image visualization, image registration, or dMRI  
 923 processing and tractography. medINRIA was initially developed by the Asclepios Project Team, IN-  
 924 RIA, France. A new version of medINRIA is being jointly developed by the Asclepios, Athena, Parietal  
 925 and the Visages INRIA Project Teams. It also has a new website at <http://med.inria.fr/>

926 **Key Features:** Log-Euclidean metric, HARDI/ODF, Fiber Tracking.

927 [BrainVISA/Anatomist](http://brainvisa.info/) <http://brainvisa.info/>

928 BrainVISA/Anatomist is developed by the Institut Fédératif de Recherche no.49, France.

- 930 • BrainVISA is a software, which embodies an image processing factory. A simple control panel allows  
 931 the user to trigger sequences of treatments on series of images. These treatments are performed by  
 932 calls to command lines provided by different laboratories. These command lines, hence, are the  
 933 building blocks on which are built the assembly lines of the factory.
- 934 • Anatomist is a visualization software, which main originality is a generic module dedicated to  
 935 structural data, namely sets of objects linked one another into a graph structure. These objects  
 936 may be cortical folds inferred from T1 weighted MR data, fiber bundles inferred from MR diffusion  
 937 weighted data, activated clusters inferred from Statistical Parametric Maps, etc... This module  
 938 includes a nomenclature control panel, which can drive several brains simultaneously. Anatomist  
 939 provides also some tools to easily map Statistical Parametric Maps on 3D renderings of the brain,  
 940 inflated meshes of the cortical surface, etc... Finally, a manual drawing toolbox can be used for  
 941 various purpose.

942 **Key Features:** toolboxes for T1-MRI, dMRI (DTI, QBI), fMRI, MEG/EEG, etc.

943 [FMRIB Software Library \(FSL\)](http://www.fmrib.ox.ac.uk/fsl/index.html) <http://www.fmrib.ox.ac.uk/fsl/index.html>

944 FSL is a comprehensive library of analysis tools for fMRI, MRI and DTI brain imaging data. FSL  
 945 is written mainly by members of the Analysis Group, fMRIB, Oxford, UK. FSL runs on Apple and  
 946 PCs (Linux and Windows), and is very easy to install. Most of the tools can be run both from the  
 947 command line and as GUIs ("point-and-click" graphical user interfaces).

948 **Key Features:** Diffusion toolbox contains tools for low-level diffusion parameter reconstruction and  
 949 probabilistic tractography, including crossing-fiber modelling. It is also capable of tract-based spatial  
 950 statistics – voxel-wise analysis of multi-subject diffusion data.

951 [Camino Diffusion MRI Toolkit](http://web4.cs.ucl.ac.uk/research/medic/camino/pmwiki/pmwiki.php) <http://web4.cs.ucl.ac.uk/research/medic/camino/pmwiki/pmwiki.php>

952 Camino is a free, open-source, object-oriented software package for analysis and reconstruction of  
 953 dMRI data, tractography and connectivity mapping. It is developed by the Microstructure Imaging  
 954 Group, University College London, UK.

955 **Key Features:** DTI, multi-tensor model, QBI, MESD/PAS-MRI, deterministic/probabilistic tractog-  
 956 raphy, synthetic data generation and more.

957 [MRI Studio An Image Processing Program](https://www.mristudio.org/) <https://www.mristudio.org/>

958 MRI Studio is an image processing program running under Windows. It is suitable for such tasks as  
 959 tensor calculation, color mapping, fiber tracking, and 3D visualization. Most of operations can be done  
 960 with only a few clicks. DTI Studio is being developed through the support of the Laboratory of Brain  
 961

Anatomical MRI and Center for Imaging Science at Johns Hopkins University, USA.

**Key Features:** DTI, Fiber-tracking and editing, 3D visualization, Region of Interesting (ROI) drawing and statistics, image registration.

**3D Slicer** <http://www.slicer.org/>

Slicer, or 3D Slicer, is a free, open source software package for visualization and image analysis. 3D Slicer is natively designed to be available on multiple platforms, including Windows, Linux and Mac Os X. 3D Slicer provides image registration, processing of DTI (diffusion tractography), an interface to external devices for image guidance support, and GPU-enabled volume rendering, among other capabilities. It is developed by the Surgical Planning Laboratory, Brigham and Women's Hospital and the Harvard Medical School, USA.

**Key Features:** Functionality for segmentation, registration and 3D visualization of multi-modal image data, advanced image analysis algorithms for DTI and fMRI, supports standard image file formats.

**MRtrix: MR tractography including crossing fibers** <http://www.nitrc.org/projects/mrtrix/>

MRtrix provides a set of tools to perform diffusion-weighted MRI white matter tractography in the presence of crossing fibers, using Constrained Spherical Deconvolution, and a probabilistic streamlines algorithm. These applications have been written from scratch in C++, using the functionality provided by the GNU Scientific Library, and gtkmm. The software is currently capable of handling DICOM and AnalyseAVW image formats, amongst others. The source code is distributed under the GNU General Public License. MRtrix is being developed by the Brain Research Institute (BRI), Melbourne, Australia.

**Key Features:** Detection of crossing fibers using Constrained Spherical Deconvolution, probabilistic streamline fiber tracking.

**The Fiber Cup Phantom Database** <http://www.lnao.fr/spip.php?rubrique79>

The Fiber Cup was originally intended to be a tractography contest at the MICCAI conference held in London in 2009. Today, the Fiber Cup is still open and is intended to provide a common dataset with known ground truth along with an evaluation methodology to compare and challenge tractography algorithms. It was developed at Neurospin, CEA, France.

**Key Features:** Provides a MR phantom containing a plethora of crossing, kissing, splitting and bending fiber configurations, acquisitions done at three b-values providing dMRI data on three q-ball shells.

## List of Acronyms

**ADC** Apparent Diffusion Coefficient

**CC** Corpus Callosum

**CNS** Central Nervous System

**CR** Corona Radiata

**CST** Corticospinal Tract

**dMRI** Diffusion Magnetic Resonance Imaging

**dNMR** Diffusion Nuclear Magnetic Resonance

**DT** Diffusion Tensor

**DTI** Diffusion Tensor Imaging

**DSI** Diffusion Spectrum Imaging

**DWI** Diffusion Weighted Image

**EAP** Ensemble Average Propagator

**EPI** Echo Planar Imaging

**FA** Fractional Anisotropy

**FRT** Funk Radon Transform

**HARDI** High Angular Resolution Diffusion Imaging

**ILF** Inferior Longitudinal Fasciculus

**MD** Mean Diffusivity

**NGP** Narrow Gradient Pulse

**NMR** Nuclear Magnetic Resonance

1018	<b>ODF</b> Orientation Distribution Function
1019	<b>PD</b> Parkinson's disease
1020	<b>PDF</b> Probability Density Function
1021	<b>PGSE</b> Pulsed Gradient Spin Echo
1022	<b>PNS</b> Peripheral Nervous System
1023	<b>QBI</b> Q-Ball Imaging
1024	<b>RA</b> Relative Anisotropy
1025	<b>SDF</b> Spherical Diffusion Function
1026	<b>SH</b> Spherical Harmonics
1027	<b>SLF</b> Superior Longitudinal Fasciculus
1028	<b>TBI</b> Traumatic Brain Injury

## 1029 References

- 1030 1. I. Aganj, C. Lenglet, G. Sapiro, E. Yacoub, K. Ugurbil, and N. Harel. Reconstruction of the orientation distribution  
1031 function in single and multiple shell Q-ball imaging within constant solid angle. *Magnetic Resonance in Medicine*,  
1032 64(2):554–566, 2010.
- 1033 2. A.W. Anderson. Measurements of fiber orientation distributions using high angular resolution diffusion imaging. *Mag-*  
1034 *netic Resonance in Medicine*, 54:1194–1206, 2005.
- 1035 3. Vincent Arsigny, Pierre Fillard, Xavier Pennec, and Nicholas Ayache. Log-Euclidean metrics for fast and simple calculus  
1036 on diffusion tensors. *Magnetic Resonance in Medicine*, 56(2):411–421, August 2006. PMID: 16788917.
- 1037 4. P. J. Basser. Inferring microstructural features and the physiological state of tissues from diffusion-weighted images.  
1038 *NMR in Biomedicine*, 8:333–344, 1995.
- 1039 5. P. J. Basser, J. Mattiello, and D. LeBihan. Estimation of the effective self-diffusion tensor from the NMR spin echo.  
1040 *Journal of Magnetic Resonance*, B(103):247–254, 1994.
- 1041 6. P. J. Basser, J. Mattiello, and D. LeBihan. MR diffusion tensor spectroscopy and imaging. *Biophysical Journal*,  
1042 66(1):259–267, 1994.
- 1043 7. P. J. Basser, S. Pajevic, C. Pierpaoli, J. Duda, and A. Aldroubi. In vivo fiber tractography using DT-MRI data.  
1044 *Magnetic Resonance in Medicine*, 44(4):625–632, October 2000.
- 1045 8. C. Beaulieu. The basis of anisotropic water diffusion in the nervous system - a technical review. *NMR in Biomedicine*,  
1046 15:435–455, 2002.
- 1047 9. T. E. J. Behrens, H. Johansen-Berg, S. Jbabdi, M. F. S. Rushworth, and M. W. Woolrich. Probabilistic diffusion  
1048 tractography with multiple fibre orientations. what can we gain? *NeuroImage*, 34(1):144–155, 2007.
- 1049 10. T.E.J. Behrens, M.W. Woolrich, M. Jenkinson, H. Johansen-Berg, R.G. Nunes, S. Clare, P.M. Matthews, J.M. Brady,  
1050 and S.M. Smith. Characterization and propagation of uncertainty in Diffusion-Weighted MR Imaging. *Magnetic*  
1051 *Resonance in Medicine*, 50:1077–1088, 2003.
- 1052 11. Denis Le Bihan, Jean-François Mangin, Cyril Poupon, C.A Clark, S. Pappata, N. Molko, and H. Chabriat. Diffusion  
1053 tensor imaging: concepts and applications. *J Magn Reson Imaging.*, 13(4):534–46, 2001.
- 1054 12. F. Bloch. Nuclear induction. *Physical Review*, 70:460–474, 1946.
- 1055 13. P. T. Callaghan. *Principles of nuclear magnetic resonance microscopy*. Oxford University Press, Oxford, 1993.
- 1056 14. H. Y. Carr and E. M. Purcell. Effects of diffusion on free precession in nuclear magnetic resonance experiments. *Physical*  
1057 *Review*, 94:630–638, May 1954.
- 1058 15. C. A. Castano-Moraga, C. Lenglet, R. Deriche, and J. Ruiz-Alzola. A Riemannian Approach to Anisotropic Filtering  
1059 of Tensor Fields. *Signal Processing [Special Issue on Tensor Signal Processing]*, 87(2):263–276, 2006.
- 1060 16. M. Catani, R.J. Howard, S. Pajevic, and D.K. Jones. Virtual in vivo interactive dissection of white matter fasciculi in  
1061 the human brain. *Neuroimage*, 17:77–94, 2002.
- 1062 17. Yi P. Chao, Chia Y. Yang, Kuan H. Cho, Chun H. Yeh, Kun H. Chou, Jyh H. Chen, and Ching P. Lin. Probabilistic  
1063 anatomical connection derived from QBI with MFACT approach. In *2007 Joint Meeting of the 6th International*  
1064 *Symposium on Noninvasive Functional Source Imaging of the Brain and Heart and the International Conference on*  
1065 *Functional Biomedical Imaging*, 2007.
- 1066 18. C. Ched'hotel, D. Tschumperlé, R. Deriche, and O. Faugeras. Constrained flows on matrix-valued functions : application  
1067 to diffusion tensor regularization. In *Proceedings of ECCV'02*, June 2002.
- 1068 19. C. Ched'hotel, D. Tschumperlé, R. Deriche, and O. Faugeras. Regularizing flows for constrained matrix-valued images.  
1069 *J. Math. Imaging Vis.*, 20(1-2):147–162, January 2004.
- 1070 20. O Ciccarelli, M Catani, H Johansen-Berg, C Clark, and A Thompson. Diffusion-based tractography in neurological  
1071 disorders: concepts, applications, and future developments. *Lancet Neurol*, 7(8):715–27, 2008.
- 1072 21. John Crank. *The Mathematics of Diffusion*. Oxford University Press, 2nd edition, 1975.
- 1073 22. J.J. Dejerine. *Anatomie des Centres Nerveux*. Paris, Rueff & Cie., 1901.
- 1074 23. Rachid Deriche, David Tschumperlé, Christophe Lenglet, and Mikaël Rousson. Variational Approaches to the Estima-  
1075 tion, Regularization and Segmentation of Diffusion Tensor Images. In Chen & Faugeras Paragios, editor, *Mathematical*  
1076 *Models of Computer Vision: The Handbook*. Springer, 2005.
- 1077 24. M. Descoteaux, E. Angelino, S. Fitzgibbons, and R. Deriche. Regularized, Fast, and Robust Analytical Q-Ball Imaging.  
1078 *Magnetic Resonance in Medicine*, 58:497–510, 2007.
- 1079 25. M. Descoteaux, R. Deriche, T. R. Knosche, and A. Anwander. Deterministic and Probabilistic Tractography Based on  
1080 Complex Fibre Orientation Distributions. *IEEE Transactions on Medical Imaging*, 28(2):269–286, 2009.

- 1081 26. Maxime Descoteaux. *High Angular Resolution Diffusion MRI: From Local Estimation to Segmentation and Tractog-*  
 1082 *raphy*. PhD thesis, Universite de Nice - Sophia Antipolis, February 2008.
- 1083 27. Q. Dong, R.C. Welsh, T.L. Chenevert, R.C. Carlos, P. Maly-Sundgren, D.M. Gomez-Hassan, and S.K. Mukherji. Clinical  
 1084 applications of diffusion tensor imaging. *Journal of Magnetic Resonance Imaging*, 19:6–18, 2004.
- 1085 28. A. Einstein. Investigations on the theory of the Brownian movement. *Ann. der Physik*, 1905.
- 1086 29. P.T. Fletcher and S. Joshi. Principal geodesic analysis on symmetric spaces: Statistics of diffusion tensors. In *Proc.*  
 1087 *Computer Vision Approaches to Medical Image Analysis*, Prague, May 2004.
- 1088 30. Henry Gray. *Gray's Anatomy of the Human Body*. LEA and FEBIGER, 1918, 1918.
- 1089 31. E.L. Hahn. Spin echoes. *Physical Review*, 80:580–594, 1950.
- 1090 32. C.P. Hess, P. Mukherjee, E.T. Han, D. Xu, and D.B. Vigneron. Q-ball reconstruction of multimodal fiber orientations  
 1091 using the spherical harmonic basis. *Magnetic Resonance in Medicine*, 56:104–117, 2006.
- 1092 33. S. Jbabdi, M.W. Woolrich, J.L.R. Andersson, and T.E.J. Behrens. A bayesian framework for global tractography.  
 1093 *NeuroImage*, 37:116–129, 2007.
- 1094 34. Heidi Johansen-Berg and Timothy E.J. Behrens. *Diffusion MRI, From quantitative measurement to in vivo neu-*  
 1095 *roanatomy*. Elsevier, 1st edition, April 2009.
- 1096 35. Enrico Kaden, Thomas R. Knosche, and Alfred Anwander. Parametric spherical deconvolution: Inferring anatomical  
 1097 connectivity using diffusion mr imaging. *NeuroImage*, 37:474–488, 2007.
- 1098 36. M.A. Koch, D.G. Norris, and M. Hund-Georgiadis. An investigation of functional and anatomical connectivity using  
 1099 magnetic resonance imaging. *NeuroImage*, 16:241–250, 2002.
- 1100 37. P.C. Lauterbur. Image formation by induced local interactions: examples employing nuclear magnetic resonance. *Nature*,  
 1101 242:190–191, 1973.
- 1102 38. M. Lazar, D.M. Weinstein, J.S. Tsuruda, K.M. Hasan, K. Arfanakis, M.E. Meyerand, B. Badie, H.A. Rowley,  
 1103 V. Haughton, A. Field, and A.L. Alexander. White matter tractography using diffusion tensor deflection. In *Human*  
 1104 *Brain Mapping*, volume 18, pages 306–321, 2003.
- 1105 39. D LeBihan and E. Breton. Imagerie de diffusion *in vivo* par résonance magnétique nucléaire. *CR Académie des*  
 1106 *Sciences*, (301):1109–1112, 1985.
- 1107 40. Christophe Lenglet. *Geometric and Variational Methods for Diffusion Tensor MRI Processing*. PhD thesis, Universite  
 1108 de Nice - Sophia Antipolis, December 2006.
- 1109 41. Christophe Lenglet, Mickaël Rousson, Rachid Deriche, and Olivier Faugeras. Statistics on the manifold of multivariate  
 1110 normal distributions: Theory and application to diffusion tensor mri processing. *Journal of Mathematical Imaging and*  
 1111 *Vision*, 25(3):423–444, October 2006.
- 1112 42. P. Mansfield. Multi-planar image formation using nmr spin echoes. *Journal of Physics C*, 10:55–58, 1977.
- 1113 43. K.D. Merboldt, W. Hanicke, and J. Frahm. Self-diffusion nmr imaging using stimulated echoes. *J. Magn. Reson.*,  
 1114 64:479–486, 1985.
- 1115 44. Ludovico Minati and Władysław P. Węglarz. Physical foundations, models, and methods of diffusion magnetic resonance  
 1116 imaging of the brain: A review. *Concepts in Magnetic Resonance Part A*, 30A(5):278–307, 2007.
- 1117 45. M. Moakher. A differential geometric approach to the geometric mean of symmetric positive-definite matrices. *SIAM*  
 1118 *J. Matrix Anal. Appl.*, 26(3):735–747, April 2005.
- 1119 46. Maher Moakher and Mourad Zérai. The Riemannian Geometry of the Space of Positive-Definite Matrices and Its  
 1120 Application to the Regularization of Positive-Definite Matrix-Valued Data. *Journal of Mathematical Imaging and*  
 1121 *Vision*, 40(2):171–187, 2011.
- 1122 47. S. Mori, B.J. Crain, V.P. Chacko, and P.C.M. Van Zijl. Three-dimensional tracking of axonal projections in the brain  
 1123 by Magnetic Resonance Imaging. *Annals of Neurology*, 45(2):265–269, February 1999.
- 1124 48. G. J. M. Parker and D. C. Alexander. Probabilistic anatomical connectivity derived from the microscopic persistent  
 1125 angular structure of cerebral tissue. *Philosophical Transactions of the Royal Society, Series B*, 360:893–902, 2005.
- 1126 49. G.J.M. Parker and D.C. Alexander. Probabilistic monte carlo based mapping of cerebral connections utilising whole-  
 1127 brain crossing fibre information. In *IPMI*, pages 684–695, 2003.
- 1128 50. Ofer Pasternak, Nir Sochen, and Yaniv Assaf. Variational Regularization of Multiple Diffusion Tensor Fields. In  
 1129 Joachim Weickert, Hans Hagen, Gerald Farin, Hans-Christian Hege, David Hoffman, Christopher R. Johnson, and  
 1130 Konrad Polthier, editors, *Visualization and Processing of Tensor Fields*, Mathematics and Visualization, pages 165–  
 1131 176. Springer Berlin Heidelberg, 2006. 10.1007/3-540-31272-2\_9.
- 1132 51. Xavier Pennec, Pierre Fillard, and Nicholas Ayache. A Riemannian Framework for Tensor Computing. *International*  
 1133 *Journal of Computer Vision*, 66(1):41–66, January 2006. A preliminary version appeared as INRIA Research Report  
 1134 5255, July 2004.
- 1135 52. M. Perrin, C. Poupon, Y. Cointepas, B. Rieul, N. Golestani, C. Pallier, D. Riviere, A. Constantinesco, D. Le Bihan,  
 1136 and J.-F. Mangin. Fiber tracking in q-ball fields using regularized particle trajectories. In *Information Processing in*  
 1137 *Medical Imaging*, pages 52–63, 2005.
- 1138 53. C. Pierpaoli, P. Jezzard, P.J. Basser, A. Barnett, and G. Di Chiro. Diffusion Tensor MR imaging of human brain.  
 1139 *Radiology*, 201:637–648, 1996.
- 1140 54. C. Poupon. *Détection des faisceaux de fibres de la substance blanche pour l'étude de la connectivité anatomique*  
 1141 *cérébrale*. PhD thesis, Ecole Nationale Supérieure des Télécommunications, December 1999.
- 1142 55. K. Pribam and P. MacLean. Neuronographic analysis of medial and basal cerebral cortex. *J. of Neurophysiology*,  
 1143 16:324–340, 1953.
- 1144 56. E.M. Purcell, H.C. Torrey, and R.V. Pound. Resonance absorption by nuclear magnetic moments in a solid. *Physical*  
 1145 *Review*, 69:37–38, 1946.
- 1146 57. Peter Savadjiev, Jennifer Campbell, Maxime Descoteaux, Rachid Deriche, G. B. Pike, and K. Siddiqi. Disambiguation of  
 1147 complex subvoxel fibre configurations in high angular resolution fibre tractography. In *Joint Annual Meeting ISMRM-*  
 1148 *ESMRMB*, Berlin, Germany, 19-25th May 2007, to appear. International Society of Magnetic Resonance in Medicine.
- 1149 58. Jeremy D. Schmahmann, Deepak N. Pandya, Ruopeng Wang, Guangping Dai, Helen E. D'Arceuil, Alex J. de Crespigny,  
 1150 and Van J. Wedeen. Association fibre pathways of the brain: parallel observations from diffusion spectrum imaging and  
 1151 autoradiography. *Brain*, 130:630–653, 2007.



- 1152 59. N.R. Selden, D.R. Gitelman, N. Salamon-Murayama, T.B. Parrish, and M.M. Mesulam. Trajectories of cholinergic  
1153 pathways within the cerebral hemispheres of the human brain. *Brain*, 121:2249–2257, 1998.
- 1154 60. Kiran K Seunarine, P A Cook, M G Hall, K V Embleton, G J M Parker, and Daniel C Alexander. Exploiting peak  
1155 anisotropy for tracking through complex structures. *Computer Vision, IEEE International Conference on*, 0:1–8, 2007.
- 1156 61. E. O. Stejskal. Use of Spin Echoes in a Pulsed Magnetic-Field Gradient to Study Anisotropic, Restricted Diffusion and  
1157 Flow. *The Journal of Chemical Physics*, 43(10):3597–3603, 1965.
- 1158 62. E. O. Stejskal and J. E. Tanner. Spin diffusion measurements: Spin echoes in the presence of a time-dependent field  
1159 gradient. *The Journal of Chemical Physics*, 42(1):288–292, 1965.
- 1160 63. D.G. Taylor and M.C. Bushell. The spatial mapping of translational diffusion coefficients by the nmr imaging technique.  
1161 *Phys. Med. Biol.*, 30:345–349, 1985.
- 1162 64. H. C. Torrey. Bloch equations with diffusion terms. *Phys. Rev.*, 104(3):563–565, November 1956.
- 1163 65. J. D. Tournier, F. Calamante, D.G. Gadian, and A. Connelly. Direct estimation of the fiber orientation density function  
1164 from diffusion-weighted MRI data using spherical deconvolution. *NeuroImage*, 23:1176–1185, 2004.
- 1165 66. Antonio Tristan-Vega, C. F. Westin, and Santiago Aja-Fernandez. A new methodology for the estimation of fiber  
1166 populations in the white matter of the brain with the Funk-Radon transform. *NeuroImage*, 49:1301–1315, 2010.
- 1167 67. D. Tuch. *Diffusion MRI of Complex Tissue Structure*. PhD thesis, Harvard University and Massachusetts Institute of  
1168 Technology, 2002.
- 1169 68. D. Tuch. Q-ball imaging. *Magnetic Resonance in Medicine*, 52(6):1358–1372, 2004.
- 1170 69. D.S. Tuch, J.W. Belliveau, T.G. Reese, and V.J. Wedeen. High angular resolution imaging of the human brain. In  
1171 *Proceedings of the International Society for the Magnetic Resonance in Medicine*, Philadelphia, April 1999.
- 1172 70. Z. Wang, B. C. Vemuri, Y. Chen, and T. H. Mareci. A constrained variational principle for direct estimation and  
1173 smoothing of the diffusion tensor field from complex DWI. *IEEE Transactions on Medical Imaging*, 23(8):930–939,  
1174 2004.
- 1175 71. Van J. Wedeen. Mapping fiber orientation spectra in cerebral white matter with Fourier transform diffusion MRI. In  
1176 *In Proc. of the 8th Annual Meeting of ISMRM*, page 82, 2000.
- 1177 72. Van J. Wedeen, Patric Hagmann, Wen-Yih Isaac Tseng, Timothy G. Reese, and Robert M. Weisskoff. Mapping complex  
1178 tissue architecture with diffusion spectrum magnetic resonance imaging. *Magn. Reson. Med.*, 54(6):1377–1386, 2005.
- 1179 73. C.F. Westin, S.E. Maier, H. Mamata, A. Nabavi, F.A. Jolesz, and R. Kikinis. Processing and Visualization for Diffusion  
1180 Tensor MRI. *Medical Image Analysis*, 6(2):93–108, June 2002.
- 1181 74. T. H. Williams, N. Gluhbegovic, and J. Jew. *The human brain: dissections of the real brain*. Virtual Hospital, 1997.
- 1182 75. M.P. Young, G. Burns, and J.W. Scannell. *The Analysis of Cortical Connectivity*. Landes Bioscience, October 1995.

- 1184 Biology and Medicine
- 1185 Alzheimer's disease, vii, xxvii, xxix
- 1186 CNS, vii, viii, xxviii
- 1187 Central Nervous System (CNS), vii
- 1188 edema, xxvii
- 1189 grey matter, viii
- 1190 ischemia, xxvii
- 1191 Parkinson's disease, vii, xxvii–xxix
- 1192 PNS
- 1193 Peripheral Nervous System (PNS), viii
- 1194 schizophrenia, xxvii, xxix
- 1195 Traumatic Brain Injury (TBI), xxviii
- 1196 white matter, viii, xxvii, xxix
- 1197 association tract, viii, ix
- 1198 Cingulum, ix
- 1199 commissural tract, viii, ix
- 1200 Corona Radiata (CR), ix
- 1201 Corpus Callosum (CC), ix, xxvi
- 1202 Corticospinal Tract (CST), ix, xxi, xxvi
- 1203 fiber, viii, xvii, xx, xxi, xxv, xxvi, xxix
- 1204 Inferior Longitudinal Fasciculus (ILF), ix
- 1205 projection tract, viii, ix
- 1206 Superior Longitudinal Fasciculus (SLF), ix, xxvi
- 1207 Computer Science
- 1208 level-set approach, xxiv
- 1209 Log-Euclidean metric, xxiii
- 1210 regularization, xxii
- 1211 Riemannian metric, x, xxii–xxiv, xxix
- 1212 segmentation, xxii, xxiv, xxix
- 1213 Signal-to-Noise Ratio (SNR), xxviii
- 1214 Mathematics
- 1215  $Sym_n^+$ , xxii, xxix
- 1216 Bayesian, xxvi
- 1217 eigenvalues, xix
- 1218 eigenvectors, xix, xx, xxv
- 1219 Fourier Transform, xvii, xx
- 1220 Funk Radon Transform (FRT), xxii
- 1221 Kullback-Leibler divergence, xxiv
- 1222 Monte Carlo, xxvi, xxvii
- 1223 positive definite, xviii, xxii, xxiii
- 1224 Ricci curvature tensor, xxv
- 1225 Runge-Kutta, xxvi
- 1226 Spherical Harmonics, xxii
- 1227 symmetric, xviii, xix, xxii, xxiii
- 1228 Physics and Biophysics
- 1229 ADC, xviii, xxvii
- 1230 Apparent Diffusion Coefficient (ADC), xviii
- 1231 anisotropy, ix, xiv, xv, xvii–xx, xxix
- 1232 Bloch equation, xii, xv
- 1233 Bloch-Torrey equation, xv, xvi
- 1234 Brownian motion, xiii, xiv, xxix
- 1235 covariance tensor, xiv, xv
- 1236 diffusion, xiii–xv, xxix
- 1237 free, xiv, xv
- 1238 self, xiv, xv
- 1239 diffusion coefficient, xiii–xviii
- 1240 diffusion equation, xiii, xiv
- 1241 diffusion propagator, xvii
- 1242 dMRI, vii, ix, xvii, xviii, xxii, xxviii, xxix
- 1243 Diffusion MRI (dMRI), vii, xxii, xxvii, xxix
- 1244 dNMR, xiii
- 1245 Diffusion NMR (dNMR), xiii
- 1246 DSI, ix, xx, xxi, xxv, xxix
- 1247 Diffusion Spectrum Imaging (DSI), ix, xx
- 1248 DT, xvii, xix, xxv, xxvii
- 1249 Diffusion Tensor (DT), xiv, xvi, xvii, xix, xx, xxiii, xxv
- 1250 DTI, ix, xviii–xx, xxii, xxv–xxvii, xxix
- 1251 **b**-matrix, xviii
- 1252 b-value, xvi
- 1253 Diffusion Tensor Imaging (DTI), ix, xviii, xx
- 1254 ellipsoid, xix, xx
- 1255 estimation, xviii, xxiii
- 1256 microstructure from, xix
- 1257 DWI, xviii
- 1258 Diffusion Weighted Image (DWI), xvii, xviii
- 1259 EAP, xvii, xx–xxii, xxv, xxvi, xxviii
- 1260 Echo Planar Imaging (EPI), x
- 1261 Einstein, ix, xiv, xxix
- 1262 FA, xix, xx, xxvi–xxviii
- 1263 Fractional Anisotropy (FA), xix, xx
- 1264 Fick's law, ix, xiii–xv, xxix
- 1265 gyromagnetic ratio, xi
- 1266 HARDI, xx, xxviii
- 1267 High Angular Resolution Diffusion Imaging (HARDI), xx
- 1268 isotropy, ix, xiii, xiv, xviii
- 1269 Larmor frequency, xi
- 1270 linear anisotropy, xx
- 1271 MD, xix, xxviii
- 1272 Mean Diffusivity (MD), xix
- 1273 NGP, xix, xx
- 1274 Narrow Gradient Pulse (NGP), xvi
- 1275 NMR, ix, xi
- 1276 Nuclear Magnetic Resonance (NMR), ix
- 1277 ODF, xxi, xxii, xxv–xxvii, xxix
- 1278 Orientation Distribution Function (ODF), xxi
- 1279 planar anisotropy, xx
- 1280 Pulse Gradient Spin Echo (PGSE), ix, xv–xviii
- 1281 q-space, ix, xvii, xix–xxi
- 1282 QBI, ix, xx–xxii, xxv, xxviii, xxix
- 1283 Q-Ball Imaging (QBI), ix, xxi
- 1284

- 1285 RA, xix  
1286 Relative Anisotropy (RA), xix  
1287 random walk, ix, xiv, xvi, xvii, xxix  
1288 SDF, xxv, xxvi, xxix  
1289 Spherical Diffusion Function (SDF), xxv  
1290 spherical anisotropy, xx  
1291 spin, xi  
1292 excitation phase, xi  
1293 longitudinal relaxation, xii  
1294 relaxation phase, xi  
1295 spin-lattice relaxation, xii  
1296 spin-spin relaxation, xii  
1297 T1-relaxation, xii  
1298 T2\*, xii  
1299 T2-relaxation, xii  
1300 transverse relaxation, xii  
1301 spin echo experiment, xii, xvi  
1302 Stejskal-Tanner, ix, xv, xvi, xviii, xxix  
1303 tractogram, xxvii  
1304 tractography, x, xxv, xxvi, xxix  
1305 deterministic, xxv, xxvi  
1306 probabilistic, xxv, xxvi  
1307 streamline, xxv, xxvi